

Study of the Mechanism of Lithium Insertion and Depletion in Lithium Iron Phosphate Thin Films

Untersuchung des Mechanismus des
Lithiumein- und -ausbaus in
Lithiumeisenphosphatdünnschichten

Vom Fachbereich 08 – Biologie und Chemie
der Justus-Liebig-Universität Gießen

angenommene Dissertation zur Erlangung des Grades
Doktor der Naturwissenschaften
-Dr. rer. nat.-

eingereicht von

Dipl.-Chem. Alexander Manfred Möller, geb. Braun
geboren am 22.02.1985 in Hannover

Gießen 2014

1. Gutachter: Prof. Dr. Jürgen Janek
2. Gutachter: Prof. Dr. Bernd Smarsly

Eingereicht am 16. Oktober 2014

Disputation am 8. Dezember 2014

Erklärung

Ich erkläre: Ich habe die vorgelegte Dissertation selbständig und ohne unerlaubte fremde Hilfe und nur mit den Hilfen angefertigt, die ich in der Dissertation angegeben habe. Alle Textstellen, die wörtlich oder sinngemäß aus veröffentlichten Schriften entnommen sind, und alle Angaben, die auf mündlichen Auskünften beruhen, sind als solche kenntlich gemacht. Bei den von mir durchgeführten und in der Dissertation erwähnten Untersuchungen habe ich die Grundsätze guter wissenschaftlicher Praxis, wie sie in der „Satzung der Justus-Liebig-Universität Gießen zur Sicherung guter wissenschaftlicher Praxis“ niedergelegt sind, eingehalten.

Gießen, 17. Dezember 2014

Alexander M. Möller

Acknowledgment

Financial Support

I gratefully thank the following institutions for financial support of this work:

- *Fonds der Chemischen Industrie* (FCI) for a 3 year Kekulé scholarship.
- *Bundesministerium für Bildung und Forschung* (BMBF) for financial support of the project *LiVe* under the innovation alliance *LIB2015*.
- The State of Hesse for providing the required infrastructure and further financial support.

Personal Support

This work would not have been possible without the personal support of various people of whom some should be named in particular:

- Prof. Dr. Jürgen Janek for giving me the opportunity to work in his group and for supervising this work.
- Dr. Joachim Sann for many fruitful discussions and guidance.
- Lisa Hederich and Saskia Blaufelder for help with all the clerical necessities.
- M. Sc. Patrick Schichtel and B. Sc. Matthias Geiss for their motivated work and the helpful contribution they made for this work with their respective bachelor theses.

- Dr. Jochen Reinacher and Dr. Mareike Falk for the cooperation and discussion in pursuit of an all-solid-state battery
- The workshop employees for quick help repairing defective parts and building of many customized parts.
- Dr. Boris Mogwiz for help with various technical problems on various machines.
- Dr. Bjoern Luerßen and Dr. Marcus Rohnke for all the administrative work and for fruitful discussions.
- Dr. Philipp Adelhelm for many fruitful discussions and for the initial supervision.
- All other members of the Janek Group and of the PCI for the great research environment and for a great time.
- Last but definitely not least, I thank my wife Maren for her support through this time.

Abstract

The mechanism of lithium insertion and depletion in the cathode material lithium iron phosphate (LFP) has been research subject for over a decade. Although being widely-used by now, the exact mechanism still remains unclear.

Thin film technology is a method of reducing the complexity of a system in order to study these mechanisms. Firstly, this work presents the preparation of LFP thin films with pulsed laser deposition (PLD). Galvanostatic cycling of thin films prepared on metal substrates was possible for 100 cycles without significant capacity loss. Films prepared on silicon substrates were smooth and covering. Chemical delithiation is compared to electrochemical delithiation. Thin films could still be cycled electrochemically after chemical delithiation. TEM images revealed the size of the primary particles to be less than 20 nm.

The preparation process was followed by a detailed electrochemical study via galvanostatic intermittent titration technique (GITT). The study reveals the vanishing of the miscibility gap in nano-sized LFP. This effect is attributed to the small size of the primary particles in the film. Furthermore, after the application of a current pulse a concentration gradient remains inside the film even after long relaxation times. Diffusion coefficients of the single-phase LFP were determined. A model for the mechanism of delithiation of the thin film is proposed supporting the model of meta-stable intermediate phases as has been suggested for LFP nanoparticles.

An outlook toward a cell for in operando spectroscopy is shown in the last chapter. Proof of principle studies have been conducted and a design for a cell is proposed.

Zusammenfassung

Der Mechanismus der Lithiuminsertion und -extraktion in das Kathodenmaterial Lithiumeisenphosphat (LFP) wird seit über einem Jahrzehnt erforscht. Obwohl dieses Material inzwischen häufig verwendet wird, sind die genauen Mechanismen noch immer ungeklärt.

Dünnschichttechnik ist eine Methode zur Reduktion der Komplexität eines Systems, um solche Mechanismen zu untersuchen. Zunächst wird in dieser Arbeit die Herstellung von LFP Dünnschichten mittels gepulster Laserdeposition (PLD) beschrieben. Galvanostatisches Zyklisieren von Dünnschichten auf Metallsubstraten über 100 Zyklen war ohne signifikanten Kapazitätsverlust möglich. Dünnschichten auf Siliciumsubstraten waren glatt und deckend. Chemische Delithiierung wird mit elektrochemischer Zyklisierung verglichen. Dünnschichten konnten auch nach chemischer Delithiierung noch elektrochemisch zyklisiert werden. TEM-Aufnahmen zeigen eine Primärpartikelgröße von weniger als 20 nm.

Nach der Präparation der Schichten wurden detaillierte elektrochemische Untersuchungen mittels galvanostatisch intermittierender Titrationstechnik (GITT) durchgeführt. Diese Untersuchungen zeigen ein Verschwinden der Mischungslücke in LFP-Dünnschichten aufgrund der kleinen Partikelgröße. Außerdem bleibt ein Gradient der Lithiumkonzentration auch nach langen Relaxationszeiten. Diffusionskoeffizienten des einphasigen Materials wurden bestimmt und ein Modell der Delithiierung des Dünnschichtfilms wird vorgestellt, das die in der Literatur vorgeschlagene Theorie der metastabilen Zwischenphase unterstützt.

Im Sinne eines proof of principle für in operando Spektroskopie werden im letzten Kapitel erste Experimente vorgestellt und ein Zelldesign hierfür wird vorgeschlagen.

Contents

1	Introduction and Motivation	1
1.1	Lithium Ion Batteries	1
1.2	Strategy of this Work / Why Utilize Thin Films?	2
1.3	Terminology of Time Resolved Studies	3
1.4	All-Solid-State Cells	4
2	Lithium Iron Phosphate	6
2.1	Crystal Structure and Defects	6
2.2	Phase Diagram	9
2.3	Electrochemical Properties	10
2.4	Proposed Mechanisms of Lithiation and Delithiation	10
2.4.1	Shrinking Core Model	10
2.4.2	Domino Cascade Model	11
2.4.3	Mosaic Model	11
2.4.4	Non-Equilibrium Models	13
2.4.5	Reviewing the Proposed Models	13
2.5	PLD of LiFePO_4	14
3	Experimental Methods	17
3.1	Pulsed Laser Deposition	17
3.1.1	Principles of Pulsed Laser Deposition	17
3.1.2	Target Preparation	19
3.1.3	PLD System	19
3.1.4	Thin Film Preparation	21
3.2	Structural Characterization	22

3.3	Electrochemical Characterization	23
4	Electrochemical Methods for Kinetic Studies	26
4.1	Galvanostatic Intermittent Titration Technique (GITT)	26
4.2	Critical Approximations of the GITT Equation	31
4.3	Further Quantities Measurable by GITT	32
4.4	GITT on LiFePO_4	33
5	Structural and Electrochemical Properties of LFP Thin Films	34
5.1	Thin Films on Metal Substrates	34
5.2	Thin Films on Single Crystal Substrates	38
5.2.1	Preparation	39
5.2.2	Chemical Delithiation versus Electrochemical Delithiation	39
5.2.3	Chemical Delithiation of LiFePO_4 Thin Films	40
5.2.4	Morphology of As-Deposited Thin Films	42
5.2.5	Electrochemical Characterization	46
5.3	Comparison with Thin Films Reported in Literature	49
6	GITT Measurements on LFP Thin Films	51
6.1	Experimental Procedure	51
6.2	Results	52
6.3	Discussion	56
6.4	Explaining the Observed Data	57
6.5	Diffusion Coefficient of the Disordered Phase	59
7	Imaging of the $\text{LiFePO}_4/\text{FePO}_4$ Phase Boundary	62
7.1	Deposition of LFP onto X-Ray Transparent Windows	62
7.2	Image Acquisition	63
8	Outlook - Toward In Operando Microscopy	66
8.1	Requirements for In Operando Studies	66
8.2	In Operando Cells in Literature	67
8.3	Lithography for an In Operando Micro Cell	68
8.4	Concluding Remarks	70

List of Tables	72
List of Figures	73
List of Symbols	75
List of Abbreviations	76
Bibliography	77

1 Introduction and Motivation

1.1 Lithium Ion Batteries

Batteries are a vital part of the technological world we live in today. Countless mobile applications require energy storage systems that are light and small. The major challenge is to build a device, that has a high energy density and is yet safe to be carried around. The first rechargeable lithium battery has been introduced by *SONY* in 1991 and has since been the key technology for the advancement in mobile applications.^[1] Most lithium ion batteries used today still utilize the same cell chemistry that was used in those first cells, a lithium cobalt oxide cathode and a carbon anode. A major issue in this system is the oxide on the cathodic side. Only half the lithium can be safely extracted from the material before the structure becomes unstable and decomposes. The decomposition leads to the liberation of oxygen reacting with the organic electrolyte. This issue is tolerable to some degree on the small scale of personal mobile applications but can become dangerous on the scale of applications for electric vehicles or in aviation. In January 2013 two fires broke out in the then newly delivered Dreamliner airplanes by *Boeing*.^[2] Luckily, no one was severely harmed in those incidents, however, they resulted in a big economical damage for the company.

While LiCoO_2 still is the material used in most applications, a number of other materials have been developed with each having its own advantages and disadvantages over the other materials. One of the main reasons for new developments is of course the price, with cobalt being an expensive material. However, there are some technological reasons as well. Some materials are being developed reaching for a higher energy density, e.g. by increasing the cell voltage.

Other materials are being developed in order to introduce a safer chemistry. Materials belonging to the latter group are the olivine materials LiMXO_4 , with $M = \text{Fe, Mn, Ni, Co}$ and $X = \text{P, S, Si}$. The most advanced and thus most widely used material of this group is LiFePO_4 , of which a detailed introduction will follow in chapter 2.

1.2 Strategy of this Work / Why Utilize Thin Films?

Batteries are very complex systems with many components and a lot of still unknown effects. Those systems are far from being well understood. Any effect observed in battery materials may thus be attributed to a multitude of processes. In order to understand subtle effects, the complexity of the system has to be reduced. Thin films have two major advantages in this regard. Firstly, with the short diffusion and conduction paths in a thin film of active material, conducting additives may not be necessary. Secondly, the material has a relatively well defined surface area contrasting the undefined, sometimes even porous surface area of a particle sample. The first advantage leads to the reduction of side effects overlapping the effects to be observed. The well defined surface area reduces morphological effects that sometimes make proper measurements impossible.

However, the utilization of thin films does not only bring advantages to the experimentalist. The first challenge in the task of utilizing thin films is producing films with the desired structural properties. Those films have to be deposited on suitable substrates. The required properties of the substrates depend on the design of the experiment. For electrochemical studies, the most important property is the electronic conductivity. Additionally, with the high temperatures used for the deposition of crystalline thin films, side reactions may become an issue and have to be considered in the choice of the substrate. Thirdly, the mechanical boundary conditions of thin films are completely different from particle structures. Thin films may experience severe stress during charging and discharging.

The strategy for this work was to produce thin films with a smooth surface in order to make the material accessible for spectroscopic techniques. Furthermore, the films had to be optimized for their electrochemical activity, as in operando measurements are only possible on electrochemically active material. A brief definition of the terms *in situ* and *in operando* will be given in the next section.

The objective of this work is to gain a better understanding of the mechanisms of lithium addition and depletion in the battery material LiFePO_4 . Detailed electrochemical studies on thin films will be presented in chapter 6. As an outlook for a long-term objective, a path toward spatially resolved in operando studies will be shown in chapter 8.

1.3 Terminology of Time Resolved Studies

A time resolved study of any system is generally referred to as in situ experiment. The term *in situ* translates to *in position* meaning a variation is studied in the position it takes place in. Depending on the scientific discipline the term can describe considerably different experimental set-ups.^a In material sciences in situ usually refers to a time resolved measurement while a manipulation of any kind is imposed onto the observed sample (e.g. heating, applied voltage, chemical reactions). Sometimes in situ is also used to describe the measurement of a still transforming sample well after the manipulation took place.

Contrasting the term in situ the term ex situ describes the examination of a sample after the manipulation took place while there is no further change of the measured properties. Accordingly, there is no need for temporal resolution in ex situ studies, as nothing of interest should be changing in the sample during measurement.

As it does not clarify the nature of the manipulation imposed onto the sample in situ is a somewhat general term. To be more specific regarding the nature of

^aVarious definitions for the term in situ are being used, sometimes not even including the element of temporal resolution. In physics the term may also describe a sample being prepared and studied without breaking the vacuum of the machine being used in between.

the manipulation the term *in operando* is frequently used. *In operando* refers to a time resolved measurement of a sample under operating conditions. For an electrolyte this would mean drawing a current and for a hydrogen storage material *in operando* would refer to a measurement during the insertion or extraction process.

According to the definitions given above *in operando* experiments may also be named *in situ* experiments, however, the reverse is not necessarily true. Any measurement with temporal resolution may be named an *in situ* study regardless of the imposed manipulation. The conditions for the usage of the term *in operando* are more restrictive, as the manipulation has to be the same as in the actual practical usage of the examined material. However, neither term gives any information about the spatial resolution of the measurement. In order for those terms to be used only a temporal resolution sufficient for the examined process is required.

Regarding the subject of this study, any electrochemical cycling experiment on a battery material is an *in operando* experiment. However, a simple experiment like that would usually not be termed *in operando*. Additional information has to be gained to justify the use of a supplementary descriptive term. Having an additional observation technique, e.g. x-ray diffraction, would justify that usage. One objective of the work at hand is to develop strategies toward *in operando* measurements with a good spatial resolution on battery materials.

1.4 All-Solid-State Cells

Vacuum conditions are vital for most spectroscopic techniques. In order to perform *in operando* studies on electrochemical cells all parts of the cell have to be compatible with these conditions, i.e. organic electrolytes cannot be used. One way to overcome this issue is to use solid electrolytes. As all other parts of a cell are usually solid, this leads to a cell concept where all parts are solids: an all-solid-state cell. Another option is the usage of ionic liquid electrolytes. This

approach has its own challenges that could be discussed extensively. However, this work will focus on the all-solid-state approach.

Since there is no liquid electrolyte, producing a good contact between the different components is crucial. For that reason, simply pressing the components together will not suffice. Furthermore, the kinetics of solid electrolytes is usually slower than of liquid electrolytes. Thus, the diffusion length has to be reduced by reducing the electrolyte thickness. Therefore, thin film deposition techniques are commonly used in all-solid-state approaches.

A first report of a working all-solid-state cell was published in 1993 by Bates et al.^[3,4] The cell consisted of a V_2O_5 cathode, a lithium anode, and LiPON electrolyte. The LiPON electrolyte had been published by Bates et al. one year earlier.^[5] All cell components were suitable for vacuum conditions, however, the cell design did not allow for *in operando* studies as the cathode was enclosed in the other components. It should be mentioned that spectroscopic studies were by far not the only motivation for all-solid-state cells. The main focus of research has been producing small and safe batteries for special applications. An all-solid-state cell for spectroscopic *in operando* analysis has been presented by Thißen et al.^[6] The cathode used in that setup was $LiCoO_2$. In order to have access to the cathode material, it was deposited on top of the other materials. This approach is suitable if the material to be observed can be deposited at low temperatures. A big challenge in the construction of all-solid-state cells is finding an order of depositing the components where a follow-up process does not destroy a previously deposited material. This order can be easily found for components that can be deposited at low temperatures. For components that can only be deposited at high temperatures, this can become quite a challenge. Another challenge is finding structuring techniques compatible with the deposited materials. An approach for the construction of an all-solid-state cell using lithium iron phosphate will be presented in chapter 8.

2 Lithium Iron Phosphate

The most commonly used cathode material for lithium ion batteries still is lithium cobalt oxide or derivatives hereof. Due to the toxicity, the high price, and limited resources of cobalt, usage of electrode materials based on cobalt is undesired. Accordingly, extensive research has been conducted toward alternative materials. Lithium iron phosphate (LFP) is a promising alternative to the widely-used cobalt oxide cathodes. Being already widely-used itself, it solves some of the safety issues of oxide materials, while still possessing a decent energy density. Furthermore, it is environmentally benign and utilizes the abundant element iron. The use of LFP as cathode material has first been proposed by Padhi et al. in 1997^[7] and has since been a major topic in battery research. The basic reaction scheme in an LFP electrode is as follows.



This chapter will give a brief introduction into the structural and electrochemical properties and the proposed models for the lithiation and delithiation mechanism.

2.1 Crystal Structure and Defects

LFP has an olivine structure which consists of hexagonally close-packed oxygen atoms with phosphorous atoms in one-eighth of the tetrahedral sites and metal

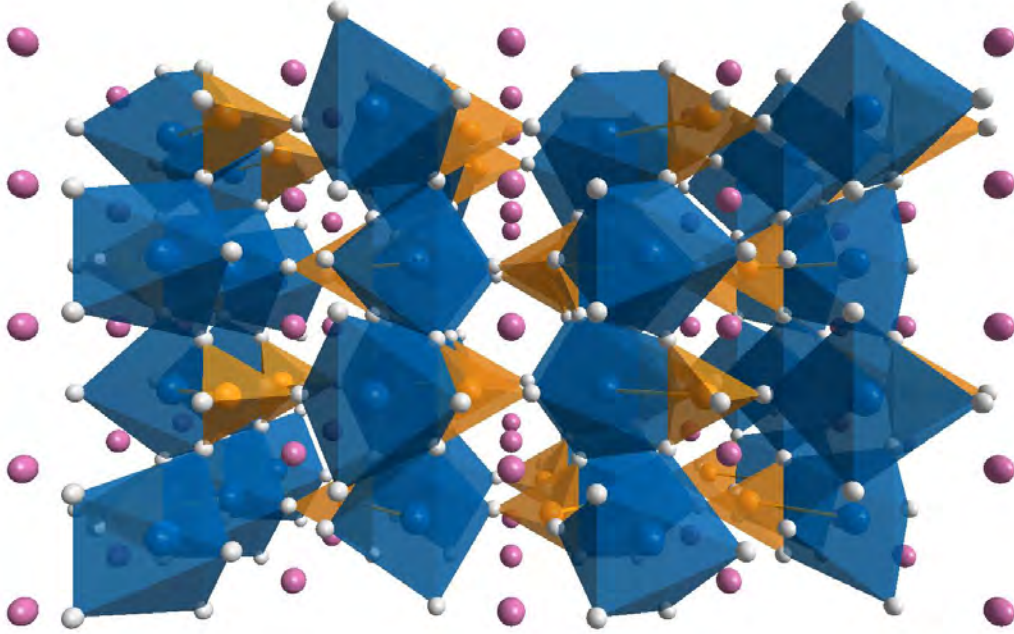


Figure 2.1: Crystal structure of LFP viewed along the lithium ion diffusion path (b -direction). blue: iron, orange: phosphorous, gray: oxygen, pink: lithium. The octahedral FeO_6 and the tetrahedral PO_4 coordination spheres are shown as well.

Table 2.1: Lattice parameters of LiFePO_4 & FePO_4 . Values from Padhi et al.^[7]

	LiFePO_4	FePO_4
Space Group	Pnma	Pnma
$a / \text{\AA}$	10.334 (4)	9.821 (1)
$b / \text{\AA}$	6.008 (3)	5.792 (1)
$c / \text{\AA}$	4.693 (1)	4.788 (1)
Volume / \AA^3	291.392 (3)	272.357 (1)

atoms in half of the octahedral sites. In contrast to the cubic analog, the spinel structure, the olivine structure has two crystallographically distinct octahedral sites with different sizes. Thus, two differently sized metal atoms will lead to an ordered olivine structure with each element occupying one of those distinct sites.^[7]

Olivine materials are one dimensional ion conductors, as the diffusion path goes along the edge-shared lithium coordination spheres. Those channels are aligned along the crystallographic *b*-axis. Lithium iron phosphate and iron phosphate both crystallize in the *Pnma* space group. The volume change upon delithiation is about 7 %. However, the cell parameters shrink along the *a* and *b*-directions by 4 to 5 %, but expand along the *c*-direction by 2 %. The structure of LFP is shown in figure 2.1. As both compounds are also found as minerals, although with manganese content, they have mineralogical names. LiFePO_4 is named triphylite and FePO_4 heterosite.

The most common defect in LFP is the Li/Fe anti-site defect.^[8,9] The formation reaction of this defect in Kröger-Vink notation is shown in equation 2.2. This kind of defect reaction is also called intersite exchange. With LFP being a one-dimensional ion conductor, anti-site defects lead to blocking of diffusion channels. Thus, the number of anti-site defects is a critical parameter in the synthesis for the performance of the obtained material.^[10,11] However, the anti-site defects tend to cluster in the iron phosphate, thus reducing the number of blocked channels. Defect clustering does not appear in manganese phosphate, which might explain the poor performance of the latter despite the identical structure.^[12]



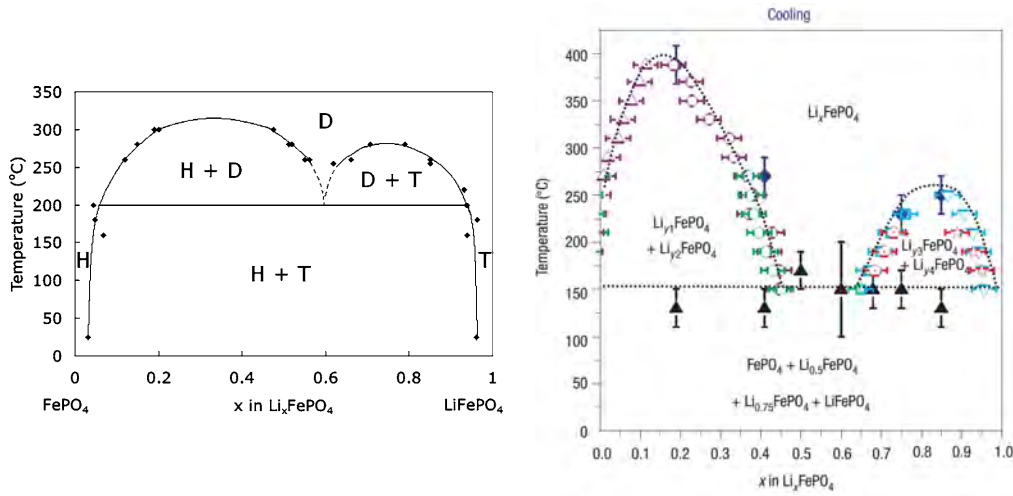


Figure 2.2: Phase diagrams of Li_xFePO_4 measured by in situ XRD. Diagram on the left from Dodd et al.^[13] Diagram on the right from Delacourt et al.^[14] The diagram by Delacourt et al. does not exhibit a triple point. This is probably due to inaccuracies of the method with short heating times in the XRD stage. Dodd et al. heated the samples in glass tubes and measured the material after quenching to room temperature. This allowed for a longer heat treatment to attain equilibrium.

2.2 Phase Diagram

Li_xFePO_4 ($0 \leq x \leq 1$) is a two phase system with the phase width of the end-phases being just a few percent. Therefore, the material exhibits a phase separation upon lithiation/delithiation. The resulting two-phase system yields a constant voltage, as predicted by Gibbs' phase rule. The phase width of the end-phases is temperature and particle size dependent. With rising temperature the phase width of the end phases becomes broader, as one would expect. However between 150 °C and 200 °C a disordered phase appears that diminishes the miscibility gap. Between 300 °C and 400 °C the miscibility gap disappears entirely in favor of a solid solution phase.^[13–15] LFP melts at around 950 °C without decomposing before.^[16,17] The phase diagrams measured by Dodd et al. and Delacourt et al. are shown in figure 2.2. Reducing the particle size broadens the phase width of the end-phases as well.^[18,19] Extrapolating the measured phase widths, the room temperature miscibility gap should disappear at a particle size of 15 nm.

2.3 Electrochemical Properties

As stated in the section above, LFP is a two-phase electrode material and has a constant voltage plateau. This plateau is at 3.4 V. The theoretical capacity is 170 mAh g^{-1} . The electronic conductivity is very low at a value of about $10^{-9} \text{ S cm}^{-1}$.^[20,21] In order to overcome the poor electronic conductivity, carbon coating was proposed by Ravet et al.^[22] Another approach to optimize the electronic transport is nanosizing of the particles to obtain short conduction paths. The advantage of nanosizing is the combined effect on the electronic and ionic transport. The employment of carbon coating also provides a reducing agent to avoid oxidation of iron during synthesis.^[23] Both methods, carbon coating and nanosizing, are being widely used, often in combination.^[24,25]

2.4 Proposed Mechanisms of Lithiation and Delithiation

Several models for the mechanism of lithium insertion and depletion have been proposed. Some of those models have been derived from electrochemical data and others from spectroscopic data. Since the beginning of this project even new models have been proposed. However, it remains unclear which of these models describes the correct mechanism.

2.4.1 Shrinking Core Model

In the initial paper Padhi et al. proposed a mechanism with a phase-transition in the shell of a particle and subsequent shrinking of the remaining core.^[7] This model was refined by Andersson et al.^[26] The electrochemical implications were studied by Srinivasan and Newman, who also proposed the name shrinking-core model.^[27] As the shrinking-core model postulates a phase boundary moving from the surface toward the core of a particle, different particle

structures should be obtained by partial cycling. This could be verified in a later study by Srinivasan and Newman.^[28] The observed cycling behavior suggested a tree-ring like structure of the particles after several partial cycles. So far, the model did not account for the one-dimensional lithium conduction of LFP. This anisotropy was incorporated into the shrinking-core model by Roscher et al.^[29] A later study by Sasaki et al. confirmed the measurements by Roscher et al. However, they inappropriately named the observation memory effect.^[30] The observed features are not a real memory effect, as they disappear after some hours of relaxation and the effect does not feature a capacity loss, but merely a shift of the charging voltage. The particle structures proposed by the presented models are shown in figure 2.3.

2.4.2 Domino Cascade Model

The shrinking-core model was challenged in 2006 by TEM measurements by Chen et al. and an EELS study by Laffont et al.^[31,32] The studies showed a FePO_4 core and a LiFePO_4 shell in delithiated particles. These findings contradicted the core-shell model, as the latter predicts a LiFePO_4 -core in delithiated particles. As Delmas et al. could show, fully lithiated and fully delithiated particles coexisted in a partially charged electrode.^[33] This led to the interpretation, that the delithiation reaction is significantly faster than the nucleation of the delithiated phase. Using the analogy of a domino being jolted and starting a cascade of all the dominoes in line falling one after another, the proposed mechanism was called domino-cascade model. This finding of Delmas et al. has been validated by an even more precise TEM study by Brunetti et al.^[34]

2.4.3 Mosaic Model

The mosaic model is similar to the shrinking-core model. In fact, it was not possible for Andersson et al. to distinguish between two possible explanations for their data, thus both models were proposed in the same publication.^[26]

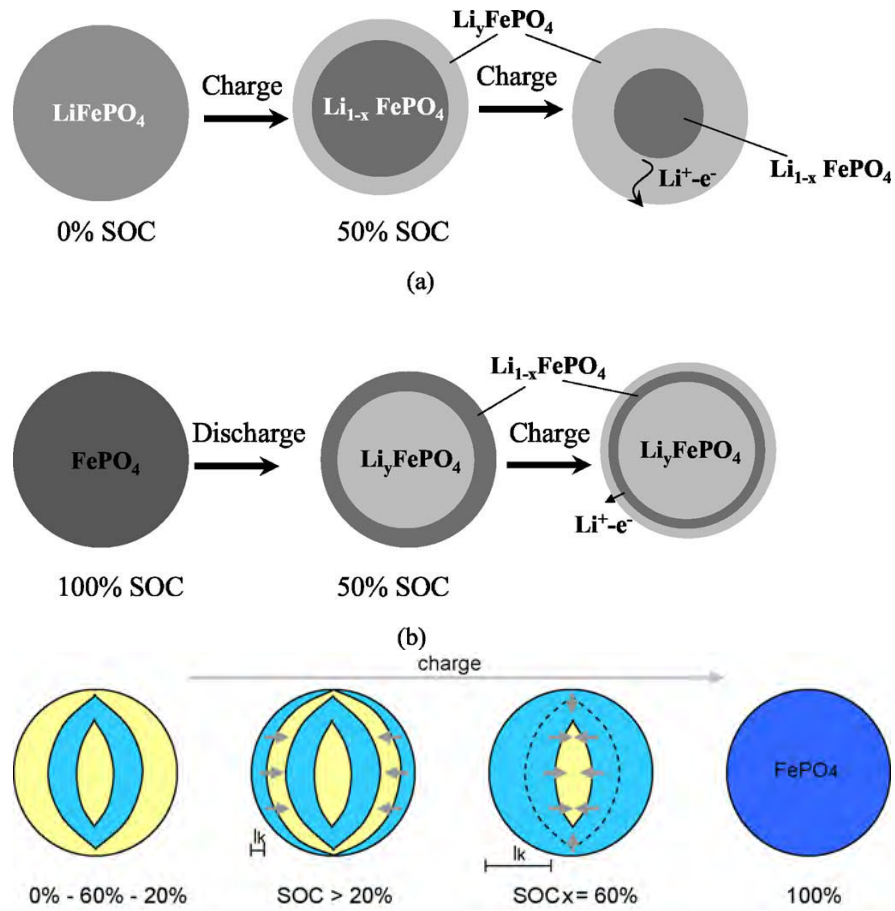


Figure 2.3: Particle structure according to the shrinking-core model as proposed by Srinivasan and Newman^[28] (top). Refined model accounting for one-dimensional lithium conduction by Roscher et al.^[29] (bottom).

According to the mosaic model the particles are not lithiated or delithiated isotropically from the surface toward the core. Rather there are numerous nucleation points in each particle with independent phase boundaries moving into the particle. This leads to a mosaic-like structure, hence the name of the model. This theory was validated by a Raman study by Ramana et al. as they found the same ratio of LiFePO_4 to FePO_4 in the shell and the core of particles with various overall lithium contents.^[35]

2.4.4 Non-Equilibrium Models

The models presented above assume a situation where local equilibrium is attained in the electrode material during charge and discharge. This does not account for any polarization or metastable intermediate phases. Accordingly, the different findings leading to the shrinking-core or the domino-cascade model could be attributed to relaxation processes after the end of the charging process. Calculations by Malik et al. showed a minimal energy configuration over the entire composition range of lithium in LFP.^[36] This minimum had a low formation energy, thus making a non-equilibrium path without phase separation possible. The phase separation would then follow after stopping the electrical current and thereby ending the externally imposed overpotential. This had previously been proposed by Meethong et al. in order to explain the electrochemical relaxation process in nano-sized LFP.^[37] The structural changes during the relaxation were studied in situ by means of x-ray diffraction by Park et al.^[38] The x-ray study showed a reorganization of the electrode particles as the phase ratio shifted toward more FePO_4 upon equilibration.

2.4.5 Reviewing the Proposed Models

Different models have been proposed for the phase change in LFP electrodes. In reviewing the studies leading to those models, there is a distinct difference between the two models subject to most of the discussion in literature. The studies

promoting the shrinking-core model utilize the interpretation of electrochemical data.^[7,26–30] The domino-cascade model is promoted by studies utilizing microscopic techniques.^[31–34] Electrochemical data give real in situ information, while electron microscopy techniques are usually performed ex situ. Thus, the different findings might be attributed to the relaxation process taking place in the electrode. Some in situ relaxation studies have been performed, accordingly leading to a model with metastable intermediate phases.^[37,38] Additionally, Lee et al. could show that an intercrystallite lithium transport takes place when small particles of FePO_4 are mixed with bigger particles of LiFePO_4 .^[39] The Lithium is transferred from the bigger particles to the smaller particles leading to a mixture of small particles of LiFePO_4 and big particles of FePO_4 .

2.5 PLD of LiFePO_4

Thin film deposition of LFP by pulsed laser deposition (PLD) was first reported by Sauvage et al. and Iriyama et al. in 2004.^[40,41] Those first thin films were very rough and not textured. The following years, a lot of work went into the optimization of the thin films and studying the influence of the structure on the performance.^[42–47,49–53] A major motivation for the research on LFP thin films has been (and still is) the pursuit of a micro-battery that would open many opportunities for special applications. However, the first demonstration of an application of LFP thin films was given by Sauvage et al. in 2008.^[48] They showed that the potential of an LFP/aqueous electrolyte half-cell is dependent on the lithium concentration in the aqueous electrolyte, making the material feasible for sensor applications. A first thorough study of the kinetic properties of PLD thin films was presented by Tang et al. in 2011.^[54]

The gravimetric charge density usually presented for particle based samples is not practical for thin films, as the mass of the film is negligible compared to the substrate mass, making a measurement of the film mass very difficult. Therefore, the volumetric capacity is usually presented. The unit commonly

2 Lithium Iron Phosphate

Table 2.2: Overview of publications with PLD preparation of LFP thin films. Substrate materials separated by a comma indicate several materials being tested, separation by a backslash indicates a substrate with an inter-layer. RT: room temperature, PA: post annealing step following the deposition, CV: cyclic voltammetry, n.a.: data not available. An overview of the film thicknesses and the film morphologies is shown in table 5.3.

Authors	Year	Substrates	Laser Fluence	Substrate Temperature	Capacity
Iriyama et al. ^[40]	2004	Pt, HOPG	$1.4 \frac{\text{J}}{\text{cm}^2}$	RT (PA@500 °C)	CV
Sauvage et al. ^[41]	2004	Si/Pt	180 mJ	600 °C	CV
Sauvage et al. ^[42]	2005	Si/Pt	$2 \frac{\text{J}}{\text{cm}^2}$	600 °C	$2.8 \frac{\mu\text{Ah}}{\text{cm}^2\mu\text{m}}$
Yada et al. ^[43]	2005	Pt, HOPG	n.a.	RT (PA@400-700 °C)	$9 \frac{\mu\text{Ah}}{\text{cm}^2\mu\text{m}}$
Song et al. ^[44]	2006	Stainless Steel, Pt	$1.4 \frac{\text{J}}{\text{cm}^2}$	700 °C	$40 \frac{\mu\text{Ah}}{\text{cm}^2\mu\text{m}}$
Sauvage et al. ^[45]	2007	Al ₂ O ₃ /Pt	$2 \frac{\text{J}}{\text{cm}^2}$	600 °C, RT (PA@500 °C)	$25 \frac{\mu\text{Ah}}{\text{cm}^2\mu\text{m}}$
Lu et al. ^[46]	2008	Si/SiO ₂ / Ti/Pt	$2 \frac{\text{J}}{\text{cm}^2}$	600 °C (PA@600 °C)	$20 \frac{\mu\text{Ah}}{\text{cm}^2\mu\text{m}}$
Matsumura et al. ^[47]	2008	Au	$1 \frac{\text{J}}{\text{cm}^2}$	600 °C	4 μAh
Sauvage et al. ^[48]	2008	Si/Pt	$2 \frac{\text{J}}{\text{cm}^2}$	600 °C	CV
Sun et al. ^[49]	2009	Ti, Si	$2 \frac{\text{J}}{\text{cm}^2}$	RT, 500 °C and 700 °C	$11 \frac{\mu\text{Ah}}{\text{cm}^2\mu\text{m}}$
Tang et al. ^[50]	2009	Ti	120 mJ	400-700 °C	$50 \frac{\mu\text{Ah}}{\text{cm}^2\mu\text{m}}$
Legrand et al. ^[51]	2010	Si	120 mJ- 160 mJ	600 °C	n.a.
Palomares et al. ^[52]	2010	Stainless Steel, Al, Si	130 mJ	RT, 500 °C	n.a.
Legrand et al. ^[53]	2011	MgO	90 mJ- 180 mJ	600 °C	n.a.
Tang et al. ^[54]	2011	Ti	120 mJ	500 °C	$35 \frac{\mu\text{Ah}}{\text{cm}^2\mu\text{m}}$

Table 2.3: Stability of conducting salts on various substrates (from Sauvage et al.^[55]).

	LiPF ₆	LiAsF ₆	LiBF ₄	LiTFSI	LiClO ₄
n-Si(001)/Pt	corroded	stable	corroded	stable	stable
Stainless Steel	corroded	corroded	corroded	corroded	stable
Ti	stable	stable	stable	stable	stable
Al	stable	stable	stable	corroded	stable

used is $\mu\text{Ah}\cdot\text{cm}^{-2}\cdot\mu\text{m}^{-1}$, with the area of the sample often being in the range of 1 cm^2 and film thicknesses mostly ranging from $0.1\text{ }\mu\text{m}$ to $1\text{ }\mu\text{m}$. The theoretical capacity of LFP is 170 mAh/g . This is equal to a volumetric capacity of $56.8\text{ }\mu\text{Ah}\cdot\text{cm}^{-2}\cdot\mu\text{m}^{-1}$. Some of the studies cited above only measured the response behavior in cyclic voltammetry without giving a capacity.^[40,41,48] Some studies did not even measure the electrochemical properties, but focused solely on structural analysis.^[51–53] Then there is one study giving capacities of the produced thin films, however, without giving a film thickness or normalizing the capacity to the film thickness.^[47] Eight of the studies cited give volumetric capacities (or those capacities can be calculated out of the data provided).^[42–46,49,50,54] Achieved capacities of PLD thin films range from $11\text{ }\mu\text{Ah}\cdot\text{cm}^{-2}\cdot\mu\text{m}^{-1}$ ^[49] to $50\text{ }\mu\text{Ah}\cdot\text{cm}^{-2}\cdot\mu\text{m}^{-1}$ ^[50], corresponding to 20 to 90 % of the theoretical capacity. An overview of those publications is presented in table 2.2.

Measuring the electrochemical properties of a sample the interaction not only of the thin film and the electrolyte has to be considered, but the substrate electrolyte interaction as well. Thin films often exhibit cracks, and no full coverage of the substrate can be assured. The interaction of several conducting salts with four different substrates has been tested by Sauvage et al.^[55] The electrolyte used was EC/DMC in all cases. Corrosion was observed with LiPF₆ and LiBF₆ salts on steel substrates and silicon substrates with platinum interlayer. Titanium and Aluminum substrates where stable with these salts. The complete results on electrolyte stability from Sauvage et al. are shown in table 2.3

3 Experimental Methods

3.1 Pulsed Laser Deposition

Physical vapor deposition techniques can be divided into two groups: equilibrium and non-equilibrium techniques. Equilibrium techniques, like thermal evaporation, are dominated by the thermodynamics of the solid-gas interface and usually do not allow for a stoichiometric transference of the target structure onto the substrate. Non-equilibrium techniques, like sputtering or pulsed laser deposition, rely on processes faster than the relaxation toward equilibrium. Thus, thermodynamics do play a role in these techniques, but they are not the dominant effect. Laser deposition techniques have been explored since the invention of lasers. However, being a purely academic subject at first, pulsed laser deposition (PLD) became a widely used technique, when high temperature superconducting oxides were reported to be deposited by this method.^[56] Since then all kinds of materials have been deposited by PLD, including insulators, polymers, and biological materials.^[57]

3.1.1 Principles of Pulsed Laser Deposition

In the pulsed laser deposition (PLD) process a target material is vaporized by a focused laser beam. The material plume produced hereby is transferred onto a substrate. The first step of the process is the ablation of the target material. The forming plume is often referred to as plasma, although less than 5 % of the

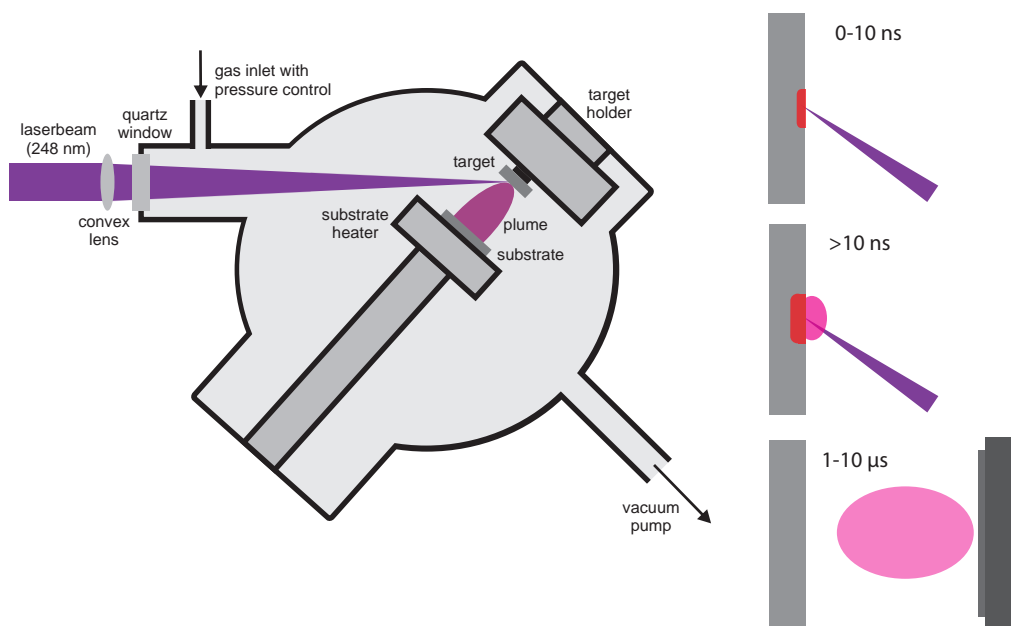


Figure 3.1: Schematic setup of a PLD chamber (left). Steps of the ablation process (right). In the first 10 ns of the laser pulse, the substrate absorbs the laser energy and the plume forms. After 10 ns and before the end of the laser pulse the plume absorbs the energy of the laser and is heated further. In the last step, the plume expands and traverses perpendicularly away from the target surface.

plume consists of ions.^[58] The forming plume is then heated by the laser during the later phase of the pulse. As the material is ejected from a solid surface, the initial direction is perpendicular to that surface. In the next phase, the plume expands with the direction still being predominantly directed away from the target. Interactions of the atoms, ions or clusters with one another or with the background gas lead to a non-directed expansion. The plume eventually reaches the substrate surface and part of the material will adsorb onto that surface. The final step is the surface diffusion that can be aided by heating the substrate. Different conditions lead to different film growth mechanisms that influence the roughness, crystallinity, and the composition of the yielded film. A basic setup of a PLD chamber and the single steps of the ablation process are shown in figure 3.1.^[59]

With the ability to deposit materials with complex stoichiometry PLD is a power-

ful technique. However, some drawbacks should be mentioned. The main issue of the PLD process is the formation of droplets. These are big particles around 1 μm in diameter that form either by splattering of molten target material carried by the expansion of the plume or by precipitation out of the supersaturated gas phase inside the plume. With film thicknesses of a few hundred nanometers, micrometer-sized particles can be a severe issue. The area that can be coated is also limited. As the plume originates from a small area and loses energy with expansion, the film in the edge regions of the substrate usually becomes thinner. Methods for reducing those issues are available, but they generally have the penalty of a much lower deposition rate.^[58]

3.1.2 Target Preparation

Carbon-free LFP powder was obtained from *Phostech Lithium*. The material was identical to the Life Power[®] P2 material, however, it was taken from the production process prior to the carbon coating step. The powder was first pressed uniaxially with a 25 mm compacting tool and a force of 20 kN. The obtained pellet was then covered with plastic wrap and put into a latex sheath. The plastic wrap had the purpose of protecting the LFP from the starch on the surface of the latex sheath, as this starch would carbonize in the sintering step. The protected pellet was then pressed isostatically at room temperature with a pressure of 3000 bar for 12 hours. Following the compacting steps, the pellet was sintered in a tube furnace under argon atmosphere at 800 °C for 24 hours. The diameter of the obtained target was about 18 mm.

3.1.3 PLD System

The PLD system was built by *SURFACE systems+technology*. The laser source was an KrF excimer laser model *Compex Pro 201 F* by *Coherent* with a wavelength of 248 nm. The size of the laser spot has been measured for several

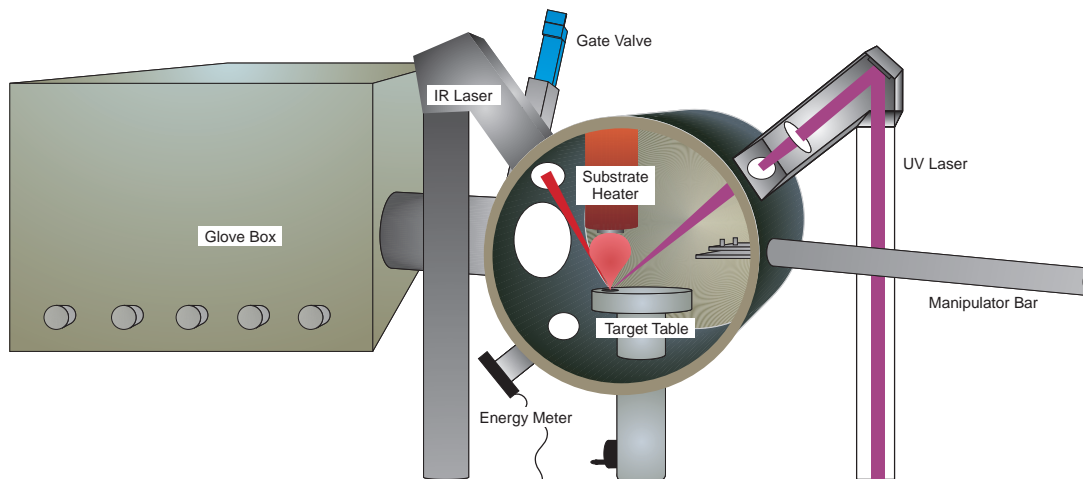


Figure 3.2: Setup of the PLD chamber.

positions of the focusing lens. The beam energy was calibrated prior to each deposition process with an energy meter on the far side of the chamber. Dividing the beam energy by the spot size yields the laser fluence on the target surface. Substrates could be fixed onto a stainless steel carrier by gluing them with silver paste, clamping them with a mask or putting them into holders with custom-fit holes. Heating of the substrate was achieved by a laser back heater or a platinum wire AC-heater. The substrate temperature was measured by a pyrometer when using the laser back heater and with a thermocouple inside a hole in the substrate holder when using the AC-heater. The gas pressure was regulated by mass flow controllers and a feedback loop of the measured pressure and the flow. Pressure measurement was done with two detectors by *Pfeiffer Vacuum*, a PKR full range gauge and a CCR gauge for an exact measurement in the pressure range commonly used in PLD processes. Targets could be placed on five positions in a target carousel. The targets could be rotated and toggled under the laser beam for a uniform ablation. The vacuum chamber was directly connected to an argon filled glovebox. The targets and the substrate holder could both be transferred into the inert gas atmosphere without exposure to air. A schematic image of the chamber is shown on figure 3.2.

3.1.4 Thin Film Preparation

The first thin films were deposited onto nickel substrates. Nickel was chosen although aluminum is usually used as current collector in commercial cells. This was due to the elevated temperatures necessary for the PLD process conflicting with the low melting point of aluminum. The metal substrates had the advantage of being good current collectors. Furthermore, they were available in a size suitable for the commonly used electrochemical testing cells, built out of 12 mm *Swagelok* T-connectors. Determining the film thickness was not feasible with these substrates, as the initial roughness was already bigger than the supposed film thickness. The substrates were glued onto a stainless steel carrier by use of silver paste.

Following those first depositions, the substrate was changed to boron doped silicon wafers since they are smooth substrates with a sufficient electric conductivity.^a The substrate temperatures were set between 600 °C and 800 °C. The laser fluence on the target was set between 2 J cm^{-2} and 3 J cm^{-2} with a frequency of 10 Hz. Argon was used as the background gas and the pressure was set to 8×10^{-3} mbar. The distance between the target and the substrate was 40 mm. A thorough study of the influence of various parameters on the film properties has been carried out by Patrick Schichtel in his bachelor thesis.^[60] The [001]-Si substrates were clamped onto the substrate carrier for deposition with the AC-heater or glued onto a carrier for depositions with the laser heater. The [111]-Si substrates were pre-cut in $1 \text{ cm} \times 1 \text{ cm}$ pieces and could thus be placed in a carrier with a matching hole. Given that the laser heater utilized light in the IR-range and silicon is transparent in that range, a stainless steel plate was put on the backside of the substrate in order to absorb the laser energy for heating.

^aElectrode materials are usually n-type conductors. Therefore using p-type substrates might lead to a p-n junction. However, due to high temperatures during PLD depositions interdiffusion will take place. This effect broadens the interface area of the p-n junction. Therefore the effect was assumed to be small and no significant influence could be observed in the experiments conducted in this study. However, the effect may become significant utilizing larger currents or impedance spectroscopy. The choice for p-doped silicon was made because of the availability of pre-cut pieces for the experimental setup.

3.2 Structural Characterization

X-Ray Diffraction

In order to examine the crystallinity and the phase purity of the obtained thin films, x-ray diffraction (XRD) was conducted. A *Siemens-D500* XRD was used. The radiation utilized was $\text{Cu-K}\alpha$.

Scanning Electron Microscopy

For analysis of the surface morphology scanning electron microscopy (SEM) was used. The available machine was the model *Merlin* from *Zeiss*. An acceleration voltage of 2 kV was chosen, since the material showed a significant radiation burn at higher voltages.

Raman Spectroscopy

Raman spectra were recorded using a spectrometer model *Senterra* by *Bruker Optik*. The wavelength of the laser was 532 nm. As Burba et al. showed, laser radiation can induce a phase change in LFP that may lead to an erroneous interpretation of the spectra.^[61] Accordingly, the lowest laser energy still yielding a decent spectrum was used for the measurements. This energy was 2 mW with a diameter of the laser spot of 10 μm .

Determination of the Film Thickness

Film thicknesses could only be determined on single crystal substrates, as the roughness of metal foils was higher than the thickness of the deposited material. The measurement of the thicknesses was achieved by use of a profilometer

model *Alpha Step IQ* by *KLA Tencor*. The measurement was conducted on the edge of the film, where the substrate was covered by a mask or clamps holding it to the carrier. Thicknesses on metal substrates were estimated by the deposition rates on single crystals at the same parameters. The film thickness in the middle of the sample is probably thicker than on the edges. Thus, the values determined by this method probably underestimate the actual film thickness. However, the data should suffice for qualitative arguments.

Transmission Electron Microscopy

TEM measurements were carried out by Dr. Frank Berkemeier at the University of Münster. The machine used was a *LIBRA 200FE* by *Zeiss*. The acceleration voltage was 200 kV. The cross section of the measured sample was prepared by cutting, grinding, and ion beam milling.

X-Ray Absorption Microscopy

Chemically delithiated samples were measured at the beamline *TwinMic* of the synchrotron *Elettra* in Trieste, Italy. The energy range of that beamline is 400 eV to 2200 eV. Accordingly, the K-edges may be measured with this technique. The spatial resolution in scanning microscopy mode is about 1 μm . The microscope has a full field imaging mode with a spatial resolution of 100 nm, this mode was not utilized however, because of the very small field of view. A detailed description of the beamline has been published by Kaulich et al.^[62]

3.3 Electrochemical Characterization

All electrochemical experiments were carried out on a *VMP3* potentiostat from *Bio-Logic*. Films on metal substrates were measured in cells made out of *Swagelok* T-connectors. These cells have a three electrode setup. Films on single

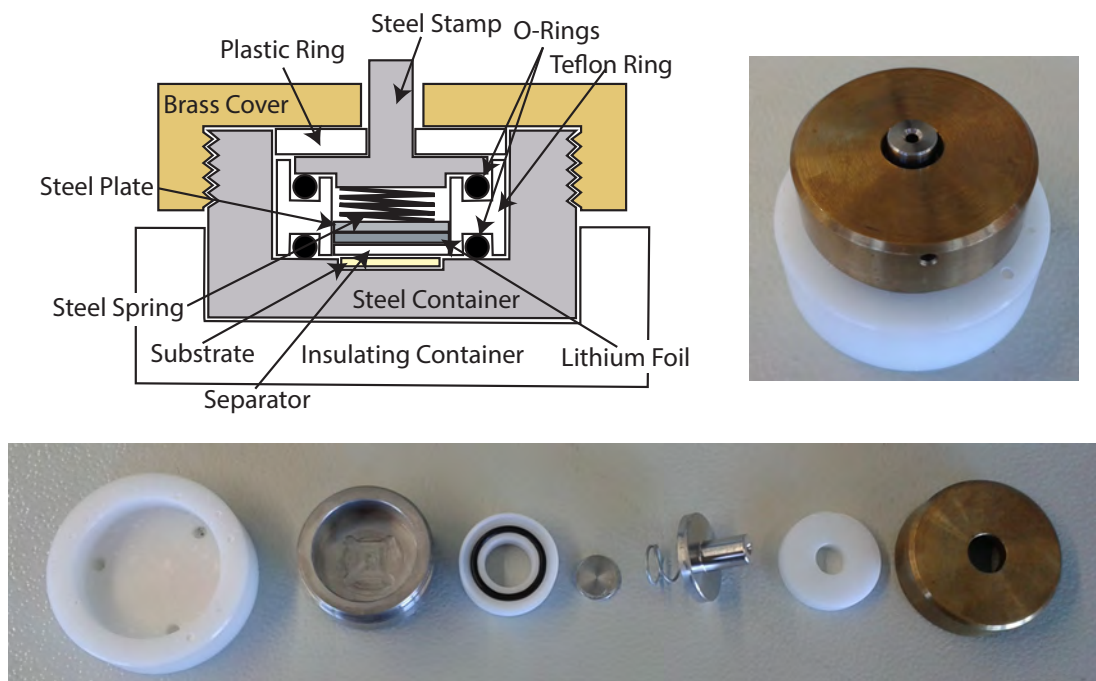


Figure 3.3: The electrochemical cell used for single crystal substrates. Schematic picture (top left), assembled cell (top right) and single parts (bottom).

crystal substrates were measured in specially designed cells with a two electrode setup. The cell for single crystal substrates is shown in figure 3.3. The electrolyte used was 1 M LiPF_6 in a 3:7 mixture of EC and DEC. If traces of water are present, the conducting salt LiPF_6 decomposes under liberation of HF. The latter dissolves LiFePO_4 . Therefore, LiBOB was used as conducting salt in the later part of this work. The electrolyte mixture was 0.1 M LiBOB in a 1:1 mixture of EC and DMC. As a separator 3 layers of separator from *Whatman* were used. The separator was drenched with 60 μL electrolyte.

The standard measurement performed with these cells was galvanostatic cycling, also referred to as chrono-potentiometry. The commonly used technique of cyclic voltammetry was not used, as the potential sweep often leads to large currents. While this is not an issue for kinetically optimized particles, thin films usually exhibit significantly slower kinetics. Thus, large current peaks as commonly seen in potential sweep measurements may destroy the thin film. In contrast, in galvanostatic cycling experiments the potential is risen until the

desired current is reached. This has the advantage of a more accurate measurement of the electrochemically active region of the potential window observed, because the inactive parts are swept through quickly while the active parts are observed with a limited current drawn through the system. Furthermore, the current was not altered with the film thickness. In particle samples, the current is often given as multiples of the current needed for a complete charge or discharge in one hour. This unit is referred to as C-rate. The capacity of an electrode is proportional to the mass of active material. In particle samples, this mass is proportional to the number of particles and thus the surface area is proportional to the capacity. In thin film samples, the surface area is about the same, regardless of the film thickness. Thus, cycling at the same C-rate for different capacities would lead to different current densities. Accordingly, the current for all galvanostatic tests was always set to a fixed value. This value was 300 nA.

4 Electrochemical Methods for Kinetic Studies

The determination of kinetic parameters is possible by a number of electrochemical techniques. The data evaluations of those techniques are based on specific approximations, which one has to be aware of. The most common methods include electrochemical impedance spectroscopy (EIS) and cyclic voltammetry (CV). Determining the diffusion coefficient by CV is possible by use of the Randle-Sevcik equation.^[63] However, this is an integral method and it only delivers an average diffusion coefficient without information about the variation with changing composition. Calculating a diffusion coefficient from EIS data can be accomplished with an equation presented by Ho et al.^[64] As with all impedance measurements, care has to be taken with the selection of the equivalent circuit for fitting the data. However, the equation mentioned is only valid for thin film electrodes, that can be fitted by the Randles equivalent circuit. In the following section a less common, but very powerful technique will be presented, the galvanostatic intermittent titration technique (GITT) as proposed and used first by Weppner and Huggins in 1977.^[65]

4.1 Galvanostatic Intermittent Titration Technique (GITT)

Titration techniques are important tools to determine composition dependent parameters. With current and time being the quantities that can be measured

most accurately, electrochemical titration is an extremely precise method.^[66] The GITT method utilizes galvanostatic steps each followed by an open circuit step. The change of composition $\Delta\delta$ during a titration step can be determined by the integral of the current over the time of the step.

$$\Delta\delta = \frac{M_B}{zm_B F} \int_0^t I dt \quad (4.1)$$

M_B is the molecular mass of compound B, z the charge of the mobile species, m_B the mass of the compound, F the Faraday constant, I the current, and t the time.

As the name of the GITT technique indicates, the current pulse is galvanostatic (i.e. a constant current is applied). Therefore, the integral can be written as the product of the current and the step time.

$$\Delta\delta = \frac{M_B}{zm_B F} I_0 \tau \quad (4.2)$$

with τ being the duration of the current pulse.

The measured potential of the electrode material depends on the concentration of the active species in the surface. Calculating that potential is only possible, if a solution of Fick's second law can be found.^a

$$\frac{\partial c_i(x,t)}{\partial t} = \tilde{D} \frac{\partial^2 c_i(x,t)}{\partial x^2} \quad (4.3)$$

Equation 4.3 is the one-dimensional version of Fick's second law with c_i being the concentration of species i , which is a function of time t and space x . \tilde{D} is the chemical diffusion coefficient, that can be dependent on the concentration.

^aActually, Fick's laws are only valid for chemical diffusion of neutral species. However, as Weppner and Huggins showed, the motion of charged species in a potential gradient can be described by equations similar to Fick's laws.^[65] As the basic equations are the same (i.e. they are mathematically identical), the known solutions for Fick's laws may be used.

4 Electrochemical Methods for Kinetic Studies

The current driven through the cell corresponds to the number of charge carriers moving through the electrode-electrolyte interface. The flux through a unit area is described by Fick's first law.

$$j_i = -\tilde{D} \frac{\partial c_i}{\partial x} \quad (4.4)$$

The flux j is a normalized quantity that corresponds to the overall current I via the electrode area S , the charge number of the mobile species z , and the Faraday constant F .

$$j_i = \frac{I}{S z_i F} \quad (4.5)$$

Applying Eq. 4.5 to Eq. 4.4 yields an expression for the surface concentration of the mobile species in the electrode.

$$I = -S z_i F \tilde{D} \frac{\partial c_i}{\partial x} \quad (x = 0) \quad (4.6)$$

Another known condition is the impermeability for ions at the interface between the electrode and the electronic current collector. Together with the assumption of a homogeneous distribution of the mobile ions this leads to the following boundary conditions for the system.

$$c_i(x, t = 0) = c_0 \quad (0 \leq x \leq L) \quad (4.7)$$

$$-\tilde{D} \frac{\partial c_i}{\partial x} \Big|_{x=0} = \frac{I}{S z_i F} \quad (t \geq 0) \quad (4.8)$$

$$\frac{\partial c_i}{\partial x} \Big|_{x=L} = 0 \quad (t \geq 0) \quad (4.9)$$

L is the material thickness, thus $x = L$ refers to the position at the interface between the electrode and the current collector. An illustration of the given boundary conditions is shown in figure 4.1.

The solution of equation 4.3 under the given boundary conditions is known.^[67]

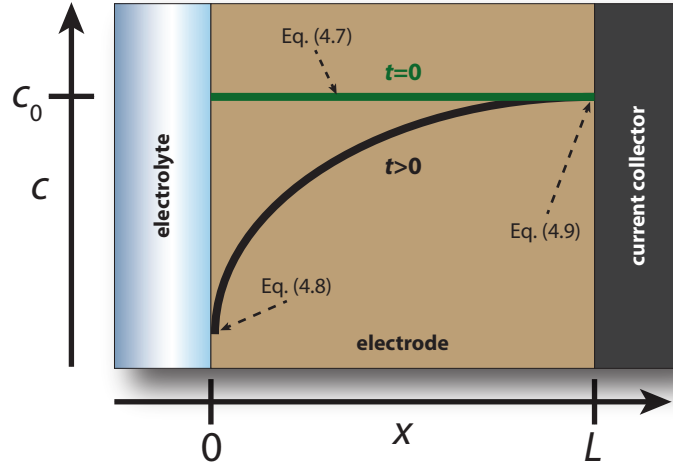


Figure 4.1: Illustration of the boundary conditions for the GITT experiment as presented in equations 4.7 through 4.9

For $x = 0$ the solution yields the following expression.

$$c_i(x = 0, t) = c_0 + \frac{2I_0\sqrt{t}}{S_{z_i}F\sqrt{\tilde{D}}} \sum_{n=0}^{\infty} \left(\text{ierfc} \left[\frac{nL}{\sqrt{\tilde{D}t}} \right] + \text{ierfc} \left[\frac{(n+1)L}{\sqrt{\tilde{D}t}} \right] \right) \quad (4.10)$$

ierfc is the integrated complementary error function defined as

$$\text{ierfc}(\lambda) = \pi^{-1/2} \exp(-\lambda^2) - \lambda + \lambda \text{erf}(\lambda) \quad (4.11)$$

The infinite sum in equation 4.10 converges toward $-\pi^{1/2}$ for big values of $L/\sqrt{\tilde{D}t}$. Therefore, the equation can be simplified for times $t \ll L^2/\tilde{D}$.

$$\frac{\partial c_i(x = 0, t)}{\partial \sqrt{t}} = -\frac{2I_0}{S_{z_i}F\sqrt{\tilde{D}\pi}} \quad (t \ll L^2/\tilde{D}) \quad (4.12)$$

The change of the composition and the concentration are related through the molar volume V_M . Neglecting the change of the molar volume with the composition, the change of the concentration is given by

$$dc_i = \frac{1}{V_M} d\delta \quad (4.13)$$

Substituting equation 4.13 into equation 4.12 and expanding by dE yields an expression for the time dependency of the cell voltage E .

$$\frac{dE}{d\sqrt{t}} = -\frac{2I_0V_M}{S_{z_i}F\sqrt{\tilde{D}}\pi} \frac{dE}{d\delta} \quad (t \ll L^2/\tilde{D}) \quad (4.14)$$

The product of elementary charge q and the Avogadro number N_A gives the Faraday constant F . Rearranging this equation yields an expression for the diffusion coefficient, where all quantities are known or measured in the GITT experiment.

$$\tilde{D} = \frac{4}{\pi} \left(\frac{V_M}{S_{z_i}F} \right)^2 \left[I_0 \left(\frac{dE}{d\delta} \right) / \frac{dE}{d\sqrt{t}} \right]^2 \quad (t \ll L^2/\tilde{D}) \quad (4.15)$$

$dE/d\delta$ is the slope of the equilibrium voltages in the titration curve. If the titration step $d\delta$ is sufficiently small, that titration step can be approximated linearly and the differential term can be replaced by the finite quantities $\Delta E_s/\Delta\delta$. $dE/d\sqrt{t}$ is the potential curve during the current pulse versus the square root of the step time. If that plot runs linearly, the differential term may be replaced by the ratio of the voltage change during the current pulse ΔE_t and the square root of the time step of that pulse $\sqrt{\tau}$.

$$\tilde{D} = \frac{4}{\pi} \left(\frac{V_M}{S_{z_i}F} \right)^2 \left[I_0 \left(\frac{\Delta E_s}{\Delta\delta} \right) / \frac{\Delta E_t}{\sqrt{\tau}} \right]^2 \quad (t \ll L^2/\tilde{D}) \quad (4.16)$$

Substituting equation 4.2 for $\Delta\delta$ yields the following expression.

$$\tilde{D} = \frac{4}{\pi\tau} \left(\frac{m_B V_M}{M_B S} \right)^2 \left[\frac{\Delta E_s}{\Delta E_t} \right]^2 \quad (t \ll L^2/\tilde{D}) \quad (4.17)$$

One last step in the process is correcting the potential values for the ohmic resistance. The IR drop can be determined by the nearly vertical part in the $E/d\sqrt{t}$ plot. The GITT procedure and the steps showing how the values are extracted from the plots are shown in figure 4.2.

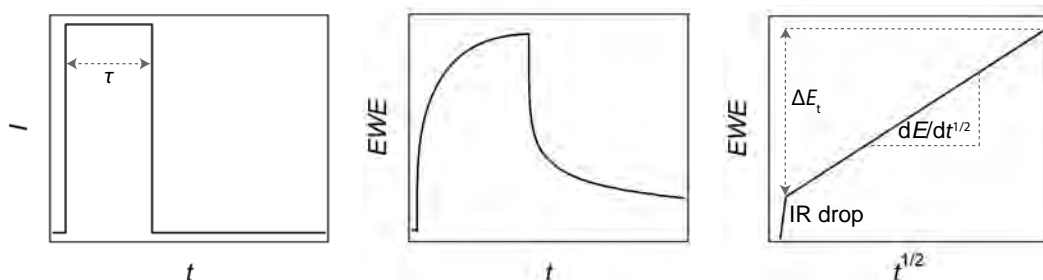


Figure 4.2: Steps of the GITT process and the extraction of data from the measurement. The externally imposed current pulse over the time step τ (left), the temporal response of the Voltage (middle) and the voltage plotted versus the square root of the step time (right).

4.2 Critical Approximations of the GITT Equation

The first approximation is the use of Fick's laws (or more precisely the equivalent equations for charged species). The known solutions of those equations are only valid for single phase systems, because a phase boundary results in a discontinuity in the concentration profile. Furthermore, the change of concentration is approximated by the measured voltage change. This approximation is also only valid for single phase systems. In two-phase systems thermodynamics causes a constant voltage as predicted by Gibbs' phase rule. Thus, the term ΔE_s in equation 4.17 is expected to become 0. This would lead to a physically meaningless diffusion coefficient of 0.

Another approximation is the short time interval in equation 4.10. However, one should note, that this is not the time of the current step but the time of the differential term in equation 4.10. As this term is approximated by the finite quantities measured, the condition holds true, as long as the plot of $dE/d\sqrt{t}$ is linear over the entire current step.

The boundary conditions and the solution of Fick's law being used require another approximation. The equations are derived for a one-dimensional diffusion geometry. Therefore, the obtained correlation is only strictly true for thin films. Furthermore, determining the surface area which is necessary for the calculation is not trivial for particle-based samples.

4.3 Further Quantities Measurable by GITT

The chemical diffusion coefficient depends on the charge carrier concentrations in the material. It is connected to the concentration independent component diffusion coefficient by the enhancement factor W . The letter W was chosen as symbol in honor of Carl Wagner. If only one ionic species is mobile and all other species can be neglected, the Wagner factor is described by equation 4.19.

$$\tilde{D} = W \cdot D_{Ki} \quad (4.18)$$

$$W = t_e \frac{\partial \ln a_i^*}{\partial \ln c_i^*} \quad (4.19)$$

The asterisks denote that the activity and concentration of the neutral species is described (i.e. describing the combined motion of ions and electrons).

If the conductivity of the material is predominantly electronic, the transference number of the electrons t_e will be about one. In this case, the enhancement factor can be determined by the slope of the steady-state titration curve.

$$\frac{\partial \ln a_i^*}{\partial \ln c_i^*} = -\frac{z_A F c_i V_M}{k T N_A} \frac{dE}{d\delta} = -\frac{z_i F (y + \delta)}{k T} \frac{dE}{d\delta} \quad (4.20)$$

Determining the enhancement factor also allows to calculate the component diffusion coefficient D_{Ki} with the relation in equation 4.18. Furthermore the geometric mean of the conductivity $\sigma_i \cdot t_e$ can be determined.

$$\sigma_i \cdot t_e = -\frac{4}{\pi} \frac{m_B V_M I_0 \Delta E_s}{M_B S^2 (\Delta E_t)^2} \quad (t \ll L^2 / \tilde{D}) \quad (4.21)$$

For a complete deduction of these equations see the original publication by Weppner and Huggins.^[65]

4.4 GITT on LiFePO_4

As noted above, the GITT equation is only valid for single phase materials. As the titration of “ Li_xFePO_4 ” easily involves two phases, the diffusion coefficient may not be determined by use of this method. Regardless thereof, diffusion coefficients of lithium in LFP using GITT measurements have been published and should be considered with caution, as they are probably incorrect.^[54,68] Although the chemical diffusion coefficient of LiFePO_4 may not be determined by GITT, the method can still yield valuable kinetic and thermodynamic information. The equilibrium voltage is determined as a function of the overall composition. Furthermore, the overpotential during and the relaxation behavior after a current pulse can be studied, leading to information about a rearrangement of the material after that pulse. Finally, the thin films prepared in this study did not exhibit a miscibility gap. Therefore the diffusion coefficients of this unusual single-phase material could be determined.

5 Structural and Electrochemical Properties of LFP Thin Films

5.1 Thin Films on Metal Substrates

At first, thin films were deposited on nickel substrates, as described in the experimental part. The deposition parameters for the thin film preparation on nickel substrates are shown in table 5.1. The thin films were characterized structurally and some electrochemical tests were carried out.

Films deposited at 500 °C had a porous structure and showed significant phase impurities in the Raman spectrum, with the impurity probably being iron oxide. All films had some lithium phosphate content as can be seen in the XRD patterns. The Raman spectra and the XRD patterns are shown in figure 5.1. The films deposited at high temperatures and with many pulses show a textured structure with a high intensity of the [210] reflection. The other films show no preferential orientation. Furthermore, the films deposited at low substrate temperatures had a porous structure, the films deposited at 700 °C were covering. This can be seen in the SEM images in figure 5.2. However, the number of films deposited on nickel substrates was too low in order to draw general conclusions. A thorough study on the influence of deposition parameters on the film properties was done by Patrick Schichtel in his bachelor thesis.^[60] The main conclusion of his thesis was that dense films can be obtained at substrate temperatures of about 700 °C.

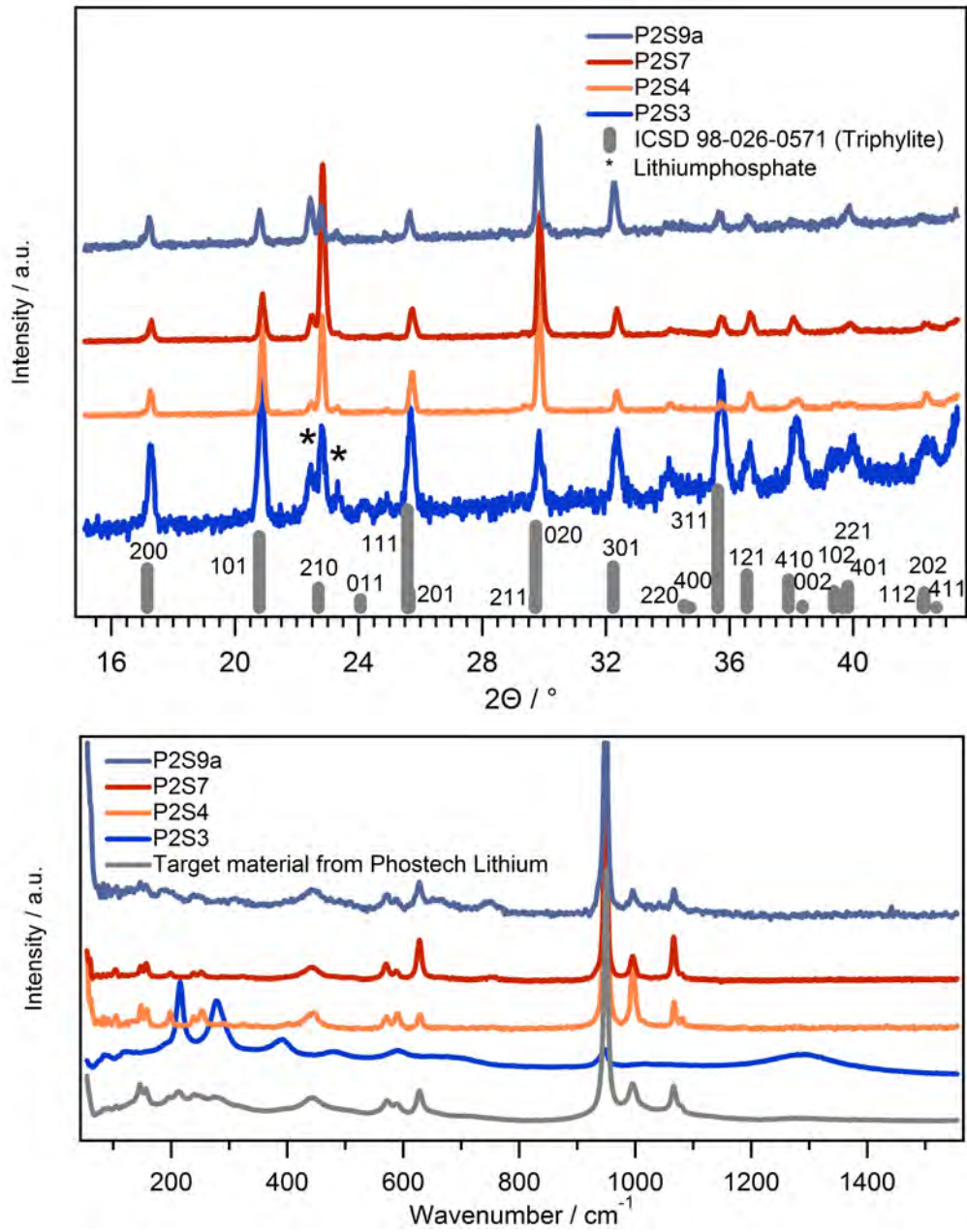


Figure 5.1: XRD patterns (top) and Raman spectra (bottom) of the thin films prepared on nickel substrates. The sample P2S3 deposited at a substrate temperature of 500 °C shows a significant amount of impurities.

5 Structural and Electrochemical Properties of LFP Thin Films

Table 5.1: Deposition Parameters for thin film preparation on nickel substrates. The background gas was 8×10^{-3} mbar argon in all cases. The frequency of the laser was set to 10 Hz. The substrate heater was the platinum wire AC-heater.

Sample Name	Substrate Temperature / °C	Laser Fluence / J cm^{-2}	Number of pulses
P2S3	500	3	18,000
P2S4	700	3	30,000
P2S5	500	3	18,000
P2S7	700	4	30,000
P2S9a	700	4	5,000

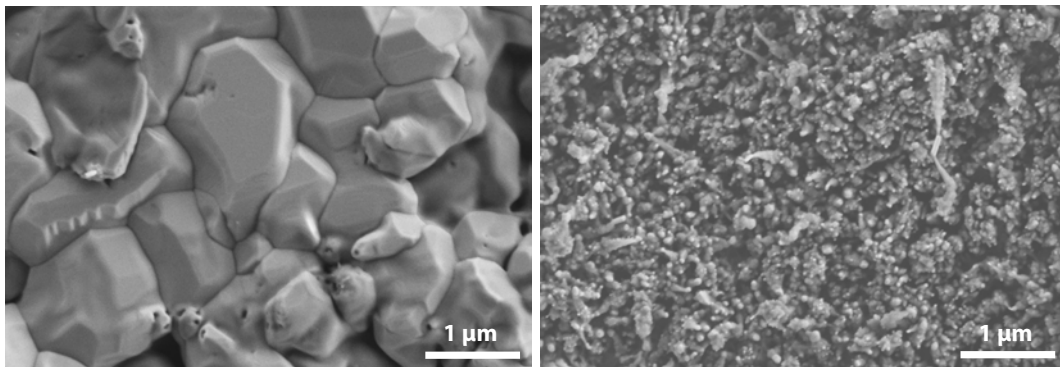


Figure 5.2: SEM images of thin films on nickel substrates. Sample P2S4 (left) was deposited at a substrate temperature of 700 °C. Sample P2S5 (right) was deposited at a substrate temperature of 500 °C

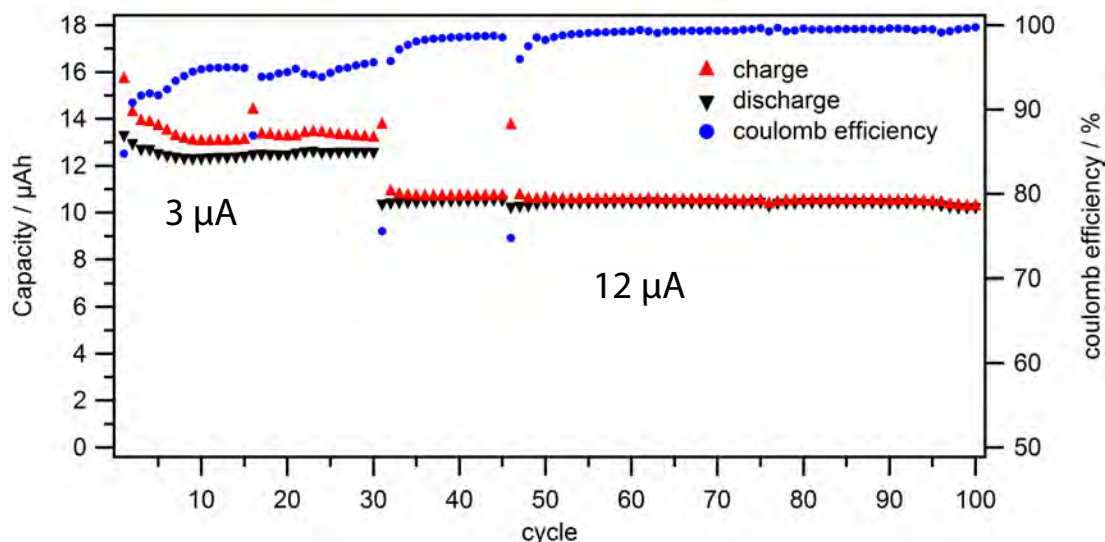


Figure 5.3: 100 galvanostatic cycles of LFP on a nickel substrate (sample P2S3). Upper and lower potential limits were set to 3.9 V and 2.9 V. Electrolyte: 1 M LiPF₆ in 3:7 EC/DEC.

Although the films presented here were not yet optimized, galvanostatic cycling over 100 cycles was possible with sample P2S3. The electrode was assembled in a 3-electrode cell with the counter and reference electrodes both being lithium metal. The charge and discharge capacities are shown in figure 5.3. The capacity can only be given in absolute values, as the film thickness could not be measured. The diameter of the substrate was 12 mm. Accordingly, the electrode area was 1.1 cm². The capacity of the cell was around 12 μAh. The first 30 cycles were charged and discharged with a current of 3 μA which corresponds to a rate of 1/4 C. In cycles 31 through 100 the current was increased to 12 μA, corresponding to 1 C. The active capacity dropped to around 10 μAh upon this increased current, however, no capacity fading was observed. The upper and lower potential limits were set to 3.9 V and 2.9 V respectively. The charge capacity jumped after each rest, however, the discharge capacity remained unaltered. This indicates a decomposition of an inter-phase and a rebuilding of that phase upon charging of the cell. It can not be determined from the data, whether that film forms on the positive or the negative electrode of the cell.

The metal substrates used in this part were easy to handle, had an excellent

5 Structural and Electrochemical Properties of LFP Thin Films

Table 5.2: Deposition Parameters for thin film preparation on silicon substrates. The background gas was 8×10^{-3} mbar argon in all cases. The frequency of the laser was set to 10 Hz.

Sample Name	Substrate	Substrate Heater	Substrate Temp. / °C	Laser Fluence / J cm ⁻²	Number of pulses	Inter-layer
E_AC_Si06a	[001]-Si	AC	700	2	5000	Ti/Pt
E_AC_Si06b	[001]-Si	AC	700	2	5000	
E_LH_Si03	[001]-Si	laser	700	3	5000	
E_LH_111Si59	[111]-Si	laser	700	2	3000	
E_LH_111Si79	[111]-Si	laser	800	2	5000	
E_LH_111Si90	[111]-Si	laser	800	2	3000	
E_LH_111Si91	[111]-Si	laser	800	2	5000	
E_LH_111Si92	[111]-Si	laser	800	2	1000	
E_LH_111Si93	[111]-Si	laser	800	2	7000	
E_LH_111Si119	[111]-Si	laser	700	2	5000	
E_AC_111Si129	[111]-Si	AC	700	2	3000	

electronic conductivity, and were available in any size desired. A big drawback of these substrates was the rough surface that made the measurement of film thicknesses impossible. Furthermore, rough substrate surfaces will never lead to the smooth and well defined interface necessary for the investigation of that interface. Thus, the next step was the deposition on very smooth substrate surfaces essentially only available on single crystal substrates.

5.2 Thin Films on Single Crystal Substrates

Silicon wafers were chosen as substrates for most depositions, as they have two major advantages. Standard wafers are already very well polished and doped wafers have an electronic conductivity sufficient for the low currents in thin film batteries. First samples were prepared on wafers with [001]-orientation (n-type). Later in this work [111]-oriented wafers (p-type) were used, as the latter were available in pre-cut pieces in the right size for the electrochemical testing cells.

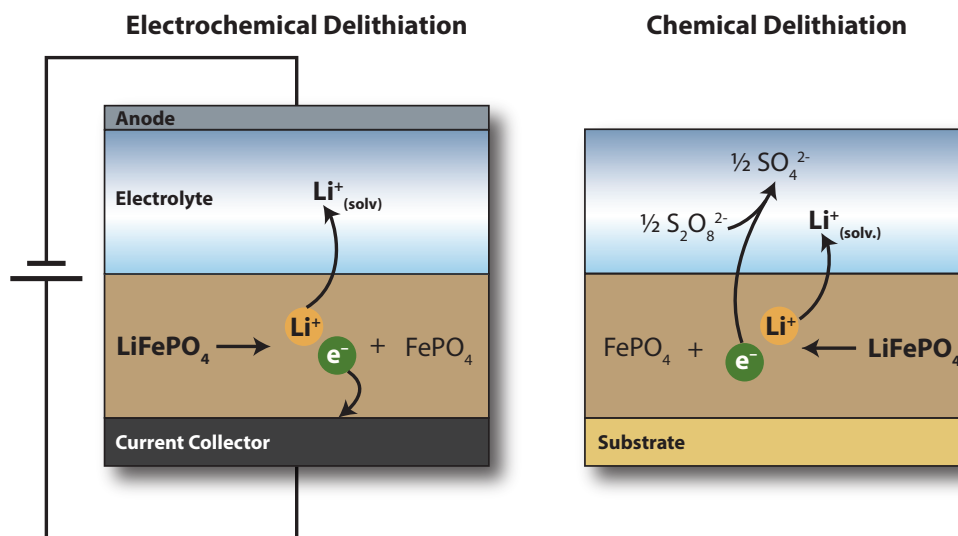


Figure 5.4: The difference between electrochemical and chemical delithiation.

5.2.1 Preparation

The films were deposited at a substrate temperature of 700 °C or 800 °C. The substrates were clamped onto the carrier with a mask that had a hole with a diameter of 12 mm. The laser fluence was set to 2 J cm^{-2} . An overview of all samples discussed in this section and the respective deposition parameters is shown in table 5.2.

5.2.2 Chemical Delithiation versus Electrochemical Delithiation

In order to examine the delithiated material, chemical delithiation was used. This method had the advantage of being independent of the preparation of functioning electrochemical cells. From a thermodynamic standpoint, it should make no difference how the potential difference for the delithiation is achieved. There are, however, some differences in the kinetics of electrochemical and chemical delithiation. Using electrochemical delithiation (e.g. chrono-potentiometry) the potential is slowly increased until a current flows. The potential is only increased so much, as to maintain a constant current. Furthermore, the

pathways of the lithium ions and the electrons are different. The lithium ions cross into the electrolyte while the electrons move toward the current collector on the other side of the particle. In chemical delithiation, the electrode is drenched in an oxidizing agent with a potential above the electrode potential. The lithium ions as well as the electrons cross the boundary toward the oxidizing agent. In addition, there is no slow increase of the potential, but a steep potential step between the electrode and the liquid. This situation is equivalent to a short circuit in an electrochemical cell. The two processes are depicted in figure 5.4.

As the differences are only of kinetic nature, thermodynamics will still drive toward the same product of the reaction. Yet, the microstructure of those products may be distinctly different. Nonetheless it is a useful method to prepare model systems for the study of the phase boundary between lithiated and delithiated materials. Electrochemical delithiation can only be performed on a conducting substrate, because the electrons have to pass through a current collector. This constraint does not apply to chemical processes, as the latter extract lithium ions and the corresponding electrons through the same pathway. In addition, chemical delithiation is a useful tool to determine, whether the material can be delithiated in the first place. If the surface is blocked for whatever reason, neither chemical nor electrochemical delithiation will be successful. Electrochemical delithiation may fail for several more reasons. Thus, chemical delithiation is an initial screening method for newly prepared materials.

5.2.3 Chemical Delithiation of LiFePO_4 Thin Films

LFP thin films were deposited onto [001]-silicon wafers. The laser fluence was 2 J cm^{-2} and the substrate temperature was 700°C . 5000 pulses were shot on the target. All other parameters are given in section 3.1.4. The given sample names were E_AC_Si06a and E_AC_Si06b. Both samples were deposited with identical parameters.

Chemical delithiation was achieved by the use of a saturated solution of $\text{K}_2\text{S}_2\text{O}_8$.

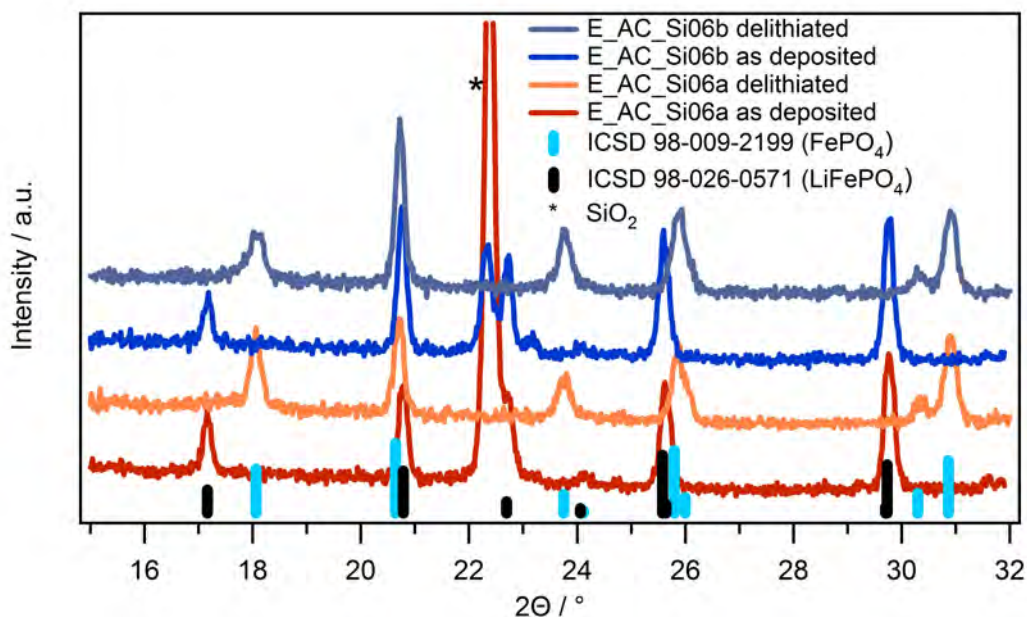


Figure 5.5: XRD patterns of as-deposited and delithiated samples. The silicon oxide reflection disappeared after the delithiation process. Delithiation was achieved with a saturated solution of $K_2S_2O_8$.

The substrate was removed from the solution after 24 hours and rinsed with demineralized water. X-ray diffraction was measured before and after the delithiation, shown in figure 5.5. The as-deposited films had the triphylite structure. The delithiated film had the heterosite structure. Prior to the delithiation, a silicon oxide film could be seen in the XRD. After the delithiation process, this oxide film had vanished. The peroxide solution should be sufficient to dissolve small amounts of silicon oxide, which would explain the disappearing reflection. However, as the SiO_x film was probably beneath the $LiFePO_4$ film, a dissolution is only possible, if the deposited film is not completely covering (i.e. protecting) the oxide film.

Despite the rather harsh conditions during chemical delithiation processes, the thin film could still be cycled in electrochemical cells after the $K_2S_2O_8$ treatment. The initial potential is at 2.8 V which is due to a thin surface film formed because of the air exposure of the sample after delithiation. However, the potential rose quickly during galvanostatic cycling with only little residual capac-

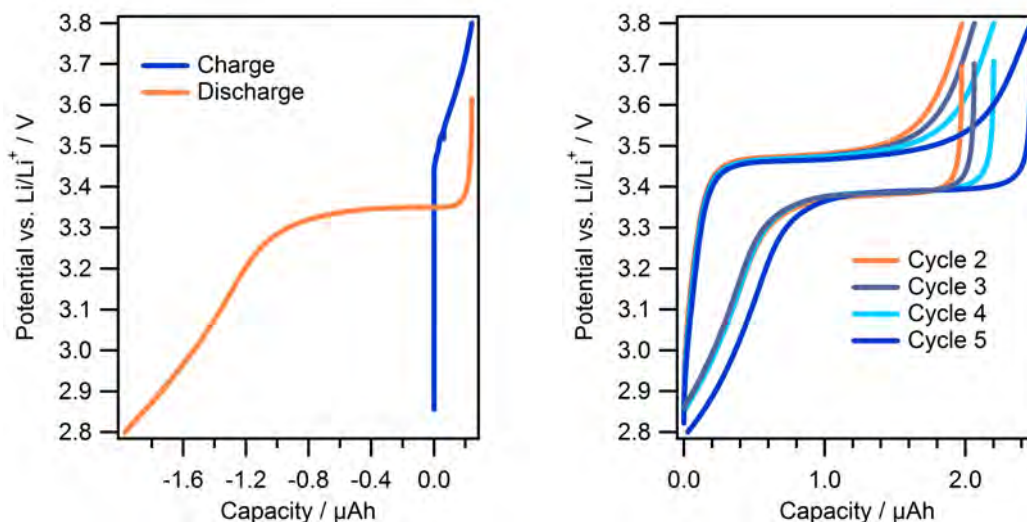


Figure 5.6: Cycling of a chemically delithiated thin film (sample E_LH_111Si119). Delithiation was achieved with a saturated solution of $K_2S_2O_8$. The current for galvanostatic cycling was set to 300 nA. The first cycle is shown on the left, beginning with the charging step. On the right the subsequent cycles 2 through 5 are shown.

ity charged in the process. The subsequent discharging step yielded a capacity of about 2 μAh . Charging and discharging of the film is possible reversibly as shown in figure 5.6.

5.2.4 Morphology of As-Deposited Thin Films

The films deposited directly on silicon substrates were not as smooth as desired and exhibited cracks. Thus, a platinum inter-layer with a titanium adhesive layer was deposited onto the substrates for some depositions. The resulting thin films were smoother and exhibited less cracks than without the inter-layer. However, at the elevated temperatures necessary for the deposition of LFP, the platinum formed an alloy with silicon. Furthermore, electrochemical cells build with thin films with platinum inter-layer were significantly less stable than cells without this inter-layer. This is probably due to the catalytic activity of platinum

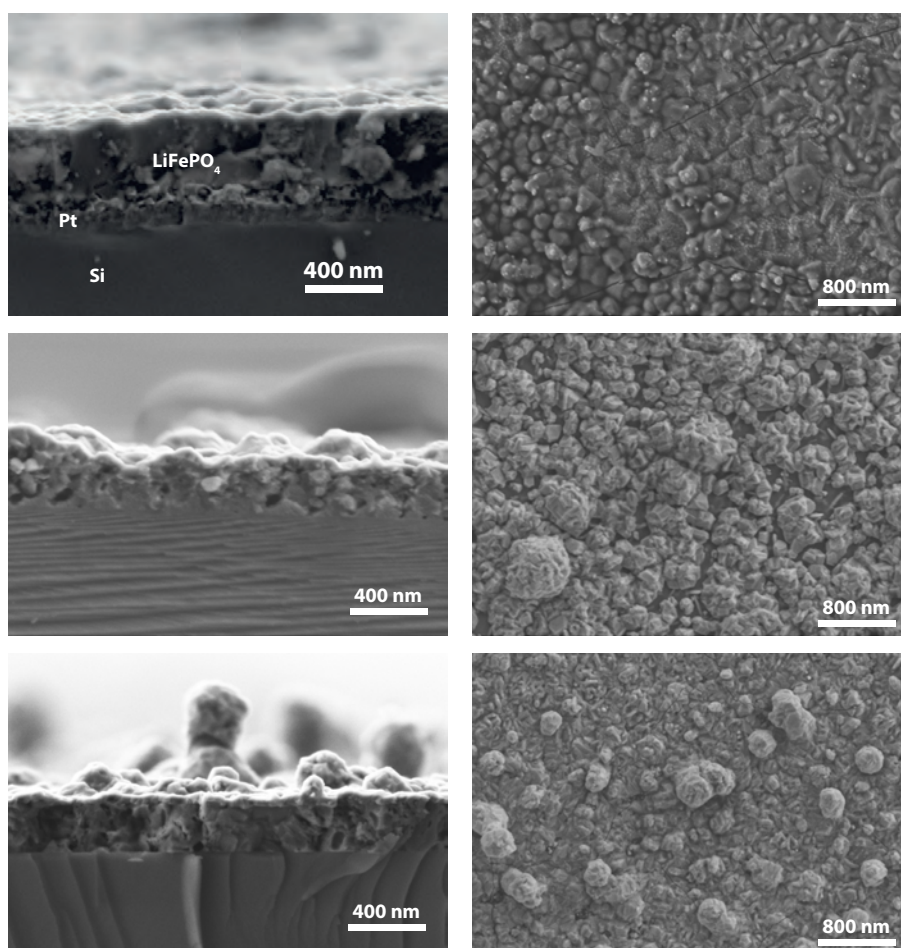


Figure 5.7: SEM images of thin film cross sections (left) and top view (right). LFP film with platinum inter-layer (top, Sample E_LH_Si03), thin film without inter-layer deposition with 3,000 pulses (middle, Sample E_LH_111Si59), thin film without inter-layer deposition with 5,000 pulses (bottom, Sample E_LH_111Si79). For deposition parameters see table 5.2 on page 38.

that lowers the electrochemical stability window of the electrolyte^a. SEM images of cross sections of films with and without platinum inter-layer are shown in figure 5.7. The cross sections were prepared by pre-cutting an edge of the silicon substrate with a glass cutter and subsequently breaking the silicon. Silicon wafers break along a straight line resulting in a well defined cross section of the film deposited thereon.

The thickness of the deposited film depends primarily on the number of laser pulses. Other factors affecting the film thickness are the morphology of the target, the laser fluence, the spot size of the laser, the pressure of the background gas, and the distance between the target and the substrate. The dependence of the film thickness on the number of pulses is shown figure 5.8. All other parameters were tried to be kept equal for all depositions. The scattering of the thicknesses especially for a large number of pulses is probably due to the fact, that the morphology of the target is changing upon ablation. Accordingly, it is not possible to keep the same surface morphology over many depositions. Using many pulses, the surface morphology of the target will also change over the course of the deposition process, thereby changing the deposition rate.

The films already showed significant texturing on the metal substrates. This effect is even stronger on the smooth single crystal substrates. The orientation is along the $\langle 210 \rangle$ -direction of the crystal, regardless of the substrate used. This implies a decoupling of the lattice parameters of the substrate and the thin film. This is probably due to an amorphous layer of LFP forming during the first deposition pulses. The XRD measurements are shown in figure 5.8. Films deposited with 3,000 to 5,000 pulses only showed the [210]-reflection. This corresponds to 213 nm and 324 nm respectively. At about 100 nm film thickness, the XRD shows only very weak reflections. A film with a thickness of 584 nm shows only little preferential orientation. Therefore, there seem to be three phases of the film growth. An amorphous inter-phase forming at the

^aThe stability of the electrolyte against oxidation is over 4 V versus Li/Li⁺. However, this value stems from cyclic voltammetry measurements and the onset point is usually defined at a current density of several $\mu\text{A}/\text{cm}^2$. Since the current density used here is only several hundred nA/cm^2 , the tolerable decomposition rate is much lower.

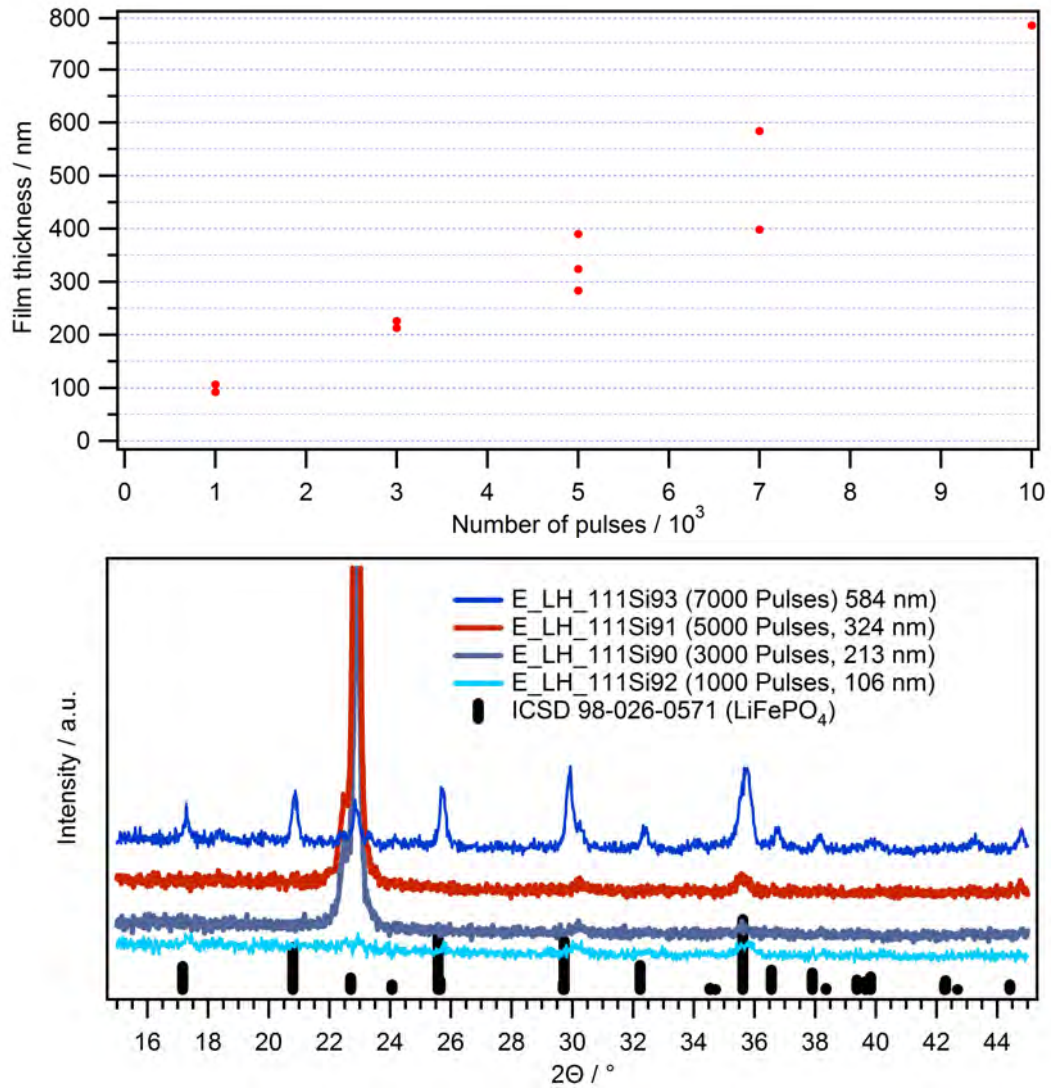


Figure 5.8: Film thickness versus number of pulses used for the deposition (top). XRDs of thin films with various thicknesses (bottom). At 100 nm the film shows only very weak reflections. At 200 nm to 350 nm the film is highly oriented. The film with a thickness of about 600 nm shows only little preferential orientation. As the thicknesses were measured at the edge of the sample, the obtained values probably underestimate the thicknesses in the middle of the sample.

substrate surface, followed by a preferentially oriented layer. This preferential orientation can only be upheld until a critical film thickness is reached, after which the film continues to grow with statistically oriented crystallites.

TEM images of sample E_AC_111Si129 show a homogeneous morphology of the film. The deposited material consists of nanocrystalline particles separated by amorphous material. The crystallite size is between 10 nm to 20 nm. The TEM images are shown in figure 5.9.

5.2.5 Electrochemical Characterization

Cells on silicon substrates were tested using a specially designed cell. For a description of the testing cell see figure 3.3 on page 24. As an electrolyte 0.1 M LiBOB dissolved in a 1:1 mixture of EC and DMC was used. Since thin films exhibit slow kinetics, the current for galvanostatic cycling was chosen at 300 nA.

The capacities of the films ranged from 1.3 μAh to 5.0 μAh . A side reaction appears in the first cycles. This leads to large irreversible capacities, however, it is unclear whether the side reaction appears on the cathode or the anode. The subsequent cycles have a decent reversibility. All films show a plateau at about 3.5 V which is characteristic for LFP. The volumetric capacity does not vary significantly depending on the deposited film thickness. The first five cycles of three samples with different film thicknesses are shown in figure 5.10. The additional discharge capacity at low potentials results from the phase width of the ordered olivine phase in nano-sized LFP. The transition from the ordered to the disordered phase could also be observed during the first charging steps of the GITT experiment presented in the next chapter.

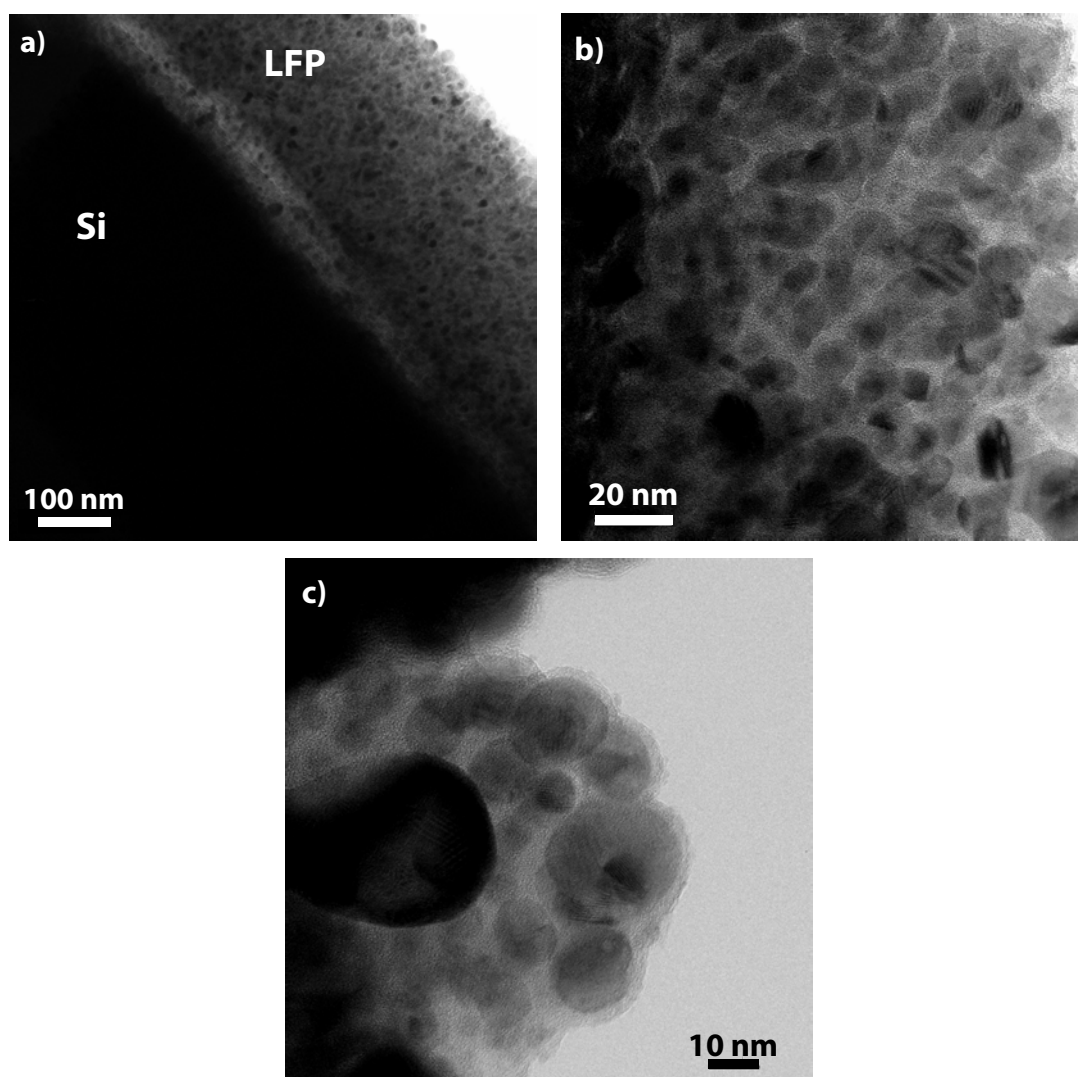


Figure 5.9: TEM images of sample E_AC_111Si129. The film consists of nanocrystalline particles with a size of 10 nm to 20 nm separated by amorphous regions. The thickness of the film is about 290 nm. a) Cross section prepared by cutting, grinding, and ion beam milling, b) higher magnification of the cross section, c) surface area of the thin film.

5 Structural and Electrochemical Properties of LFP Thin Films

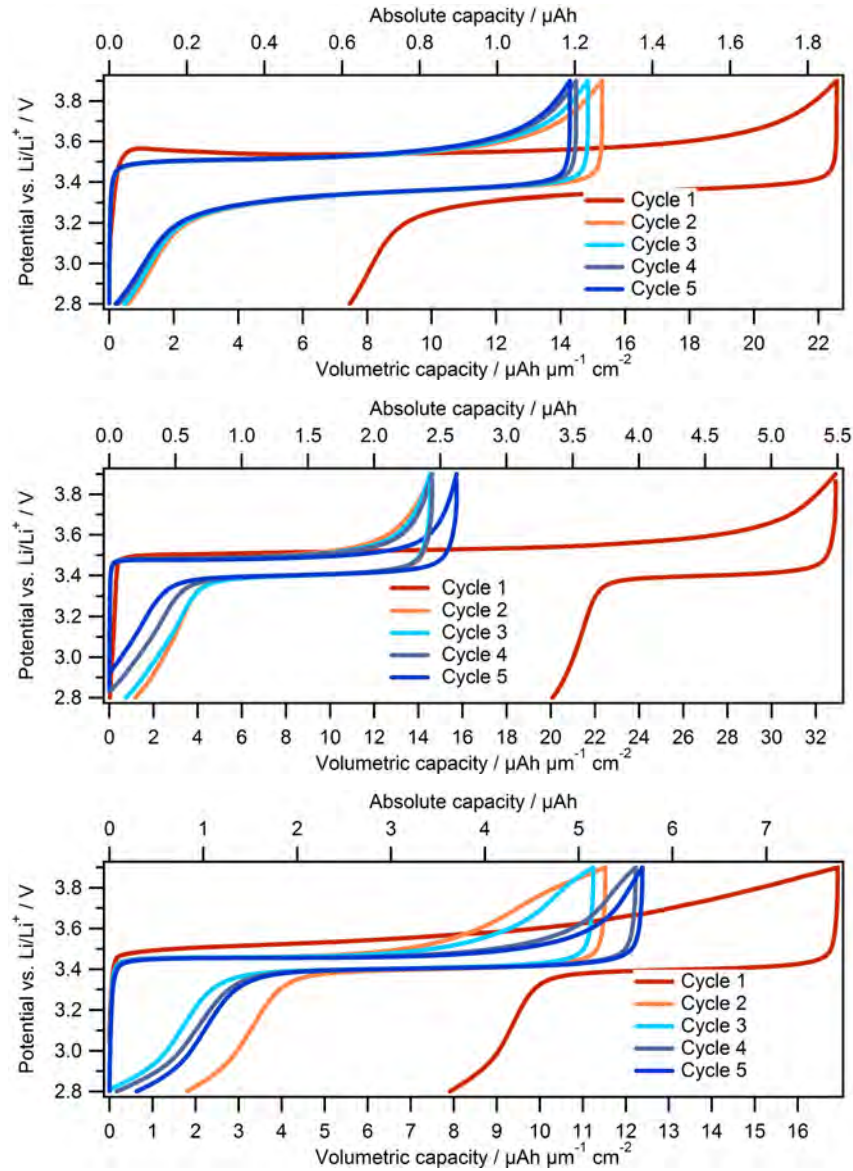


Figure 5.10: Galvanostatic cycling of thin films on silicon substrates. A side reaction occurs during the first cycle, leading to a large irreversible capacity.
 Top: Sample E_LH_111Si92, prepared with 1,000 pulses, the thickness is 106 nm.
 Middle: Sample E_LH_111Si90, prepared with 3,000 pulses, the thickness is 213 nm.
 Bottom: Sample E_LH_111Si93, prepared with 7,000 pulses, the thickness is 584 nm.

5.3 Comparison with Thin Films Reported in Literature

In order to yield a better understanding of the mechanisms of lithium insertion and depletion, spectroscopic studies are necessary. The details of those studies will be introduced in chapters 7 and 8. Thin films for the x-ray absorption studies presented in these chapters need to be covering and the thickness should be several hundred nm. Thin films presented in literature were either too thin or too rough for those studies or the electrochemical performance was not tested. An overview of the film thicknesses and morphologies is shown in table 5.3. Only one study in literature meets the criteria necessary for in situ studies.^[46] However, that study utilized composite films of LFP with carbon. Furthermore, the preparation of a smooth film was only possible with a Pt film under the LFP. Metallic inter-layers are helpful to produce smooth films, but they are prohibitive in absorption experiments like XAS presented in chapter 7. The films presented in the current work are several hundred nm thick, relatively smooth and a good electrochemical performance could be demonstrated. These properties were achieved on silicon substrates without metallic inter-layers.

Amorphous LFP has been reported in literature at the surface of uncoated LFP particles.^[69] As the amorphous material in the surface layer is electrochemically inactive, particles are usually coated (e.g. with carbon) to avoid this disordered layer. However, the amorphous layer is an electronic and ionic conductor. Thus, the amorphous matrix in the thin film is acting as a coating itself, albeit being a coating with a relatively high mass.

5 Structural and Electrochemical Properties of LFP Thin Films

Table 5.3: Film thicknesses and morphologies of PLD thin films in literature. An overview of the deposition parameters and volumetric capacities is shown in table 2.2.

Authors	Thickness / nm	Morphology
Iriyama et al. ^[40]	50	rod-like
Sauvage et al. ^[41]	300-900	many particles
Sauvage et al. ^[42]	21-600	many particles
Yada et al. ^[43]	50	roughness 20 nm
Song et al. ^[44]	75-335	very rough
Sauvage et al. ^[45]	160	rough
Lu et al. ^[46]	200	smooth, LFP-C composite material
Matsumura et al. ^[47]	n.A.	very rough
Sauvage et al. ^[48]	20-900	rough (films oriented up to 400 nm)
Sun et al. ^[49]	60	needle-like
Tang et al. ^[50]	300	very rough
Legrand et al. ^[51]	450	big particles; no electrochemical testing
Palomares et al. ^[52]	300	smooth on Si, rough on other substrates; no electrochemical testing
Legrand et al. ^[53]	150	very rough; no electrochemical testing
Tang et al. ^[54]	300	smooth on silicon, electrochemical testing only on Ti substrates

6 GITT Measurements on LFP Thin Films

Galvanostatic cycling of electrochemical systems only yields information about the respective system under polarizing conditions. Regardless of the use of a two or three electrode setup, the potentials will always be shifted under current flow. Although this effect may be small, high precision measurements of electrochemical potentials are not possible under a steady current flow. Accordingly, coulometric titration techniques are used to measure composition dependent properties. The details of the GITT technique used in this study are described in chapter 4.

6.1 Experimental Procedure

Samples for the GITT experiment were prepared on [111]-oriented p-type silicon substrates. The preparation parameters of the thin films are shown in table 6.1. The layout of the cell used for the GITT measurement is shown in figure 3.3 on page 24. The electrolyte was a 0.1 M solution of LiBOB in a 1:1 mixture of EC and DMC. For the GITT pulses a current of 300 nA was drawn through the cell. The pulse duration was 30 minutes. Each current pulse was followed by a relaxation for 10 hours. The process started with pulses charging the electrode (i.e. delithiating the LFP). Further charging pulses followed, if the electrode potential was below 3.5 V after the relaxation step. Upon reaching

6 GITT Measurements on LFP Thin Films

Table 6.1: Deposition Parameters for thin films used for GITT measurements. The background gas was 8×10^{-3} mbar argon in all cases. The frequency of the laser was set to 10 Hz.

Sample Name	Substrate	Substrate Heater	Substrate Temp. / °C	Laser Fluence / J cm^{-2}	Number of pulses
E_LH_111Si47	[111]-Si	laser	700	2	3000
E_LH_111Si75	[111]-Si	laser	800	2	5000
E_LH_111Si76	[111]-Si	laser	800	2	5000
E_LH_111Si113	[111]-Si	laser	800	2	3000

the limiting potential after relaxation, the process was reversed. The limiting potential for the discharging was 3.2 V after relaxation.

The capacity of the films was between 8 μAh and 10 μAh . The charging capacity per pulse was 0.15 μAh and the duration of one pulse plus the ensuing relaxation step was 10.5 hours. The time for one GITT experiment, including a complete charge and a complete discharge, accumulates from 46 days to 58 days depending on the total capacity of the film. The long time necessary for each experiment led to some issues with measurements being aborted for various technical reasons. Thus, not all measurements presented here were completed until the end of the discharge cycle.

6.2 Results

At a first glance, the plot of the potential versus time looks as expected with a plateau at about 3.45 V and a steep incline of the voltage near the full charge and the full discharge of the electrode. However, a detailed analysis of the data reveals some unexpected features. The GITT plot of sample E_LH_111Si113 is shown in figure 6.1.

Even after the long relaxation time of 10 hours equilibrium is apparently not reached in the electrode. The potential of the cell is not solely composition

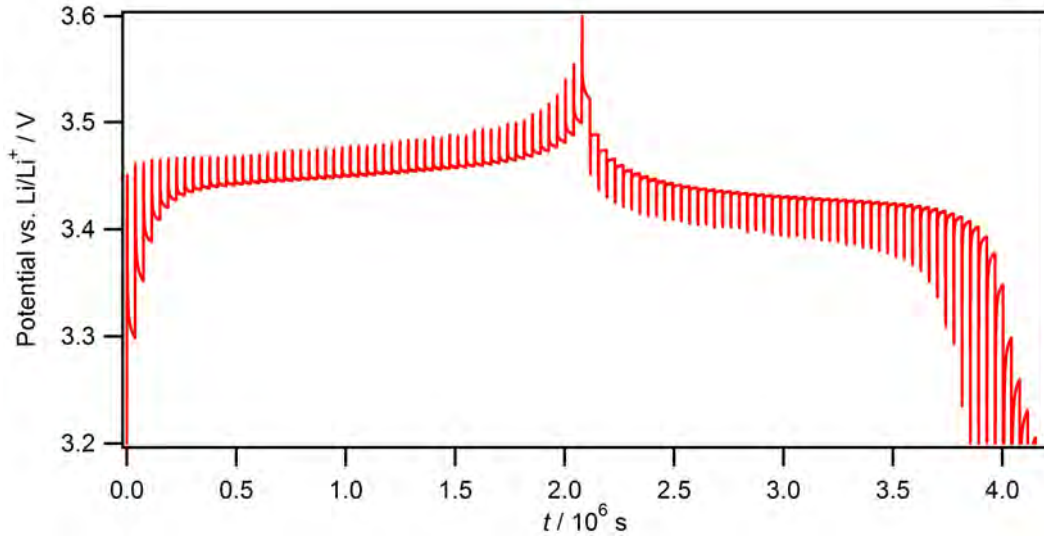


Figure 6.1: Potential versus time of sample E_LH_111Si113 during the GITT experiment. The electrolyte was 0.1 M LiBOB dissolved in a 1:1 mixture of EC:DMC. The experiment was conducted at room temperature.

dependent, but also history dependent. At the same composition, the potential differs by as much as 20 mV to 25 mV between the charging and the discharging cycle. This hysteresis occurred in all of the measured samples. Additionally, the plateau expected for a two-phase system was not a strict plateau, but exhibited a slope. This shows that the system is not in equilibrium even after a long relaxation time. The time necessary for reaching full equilibrium is probably much longer than the time of this experiment. The slope of the potential at the end of the relaxation step was less than 0.2 mV h^{-1} . The potential after the relaxation step will be referred to as *near-equilibrium potential* hereafter. Figure 6.2 shows the plots of near-equilibrium potentials and the potentials at the end of each charging pulse against the composition. As the composition cannot be determined directly, it was approximated by the capacity, with the assumption of a full delithiation after the charging cycle. The discharge capacity is about 90 % of the charging capacity. The charging capacity of sample E_LH_111Si75 was $11.0 \text{ } \mu\text{Ah}$ corresponding to a volumetric capacity of about $37 \text{ } \mu\text{Ah} \cdot \text{cm}^{-2} \cdot \mu\text{m}^{-1}$. The capacity of sample E_LH_111Si113 was $8.3 \text{ } \mu\text{Ah}$ corresponding to a volumetric capacity of about $42 \text{ } \mu\text{Ah} \cdot \text{cm}^{-2} \cdot \mu\text{m}^{-1}$.

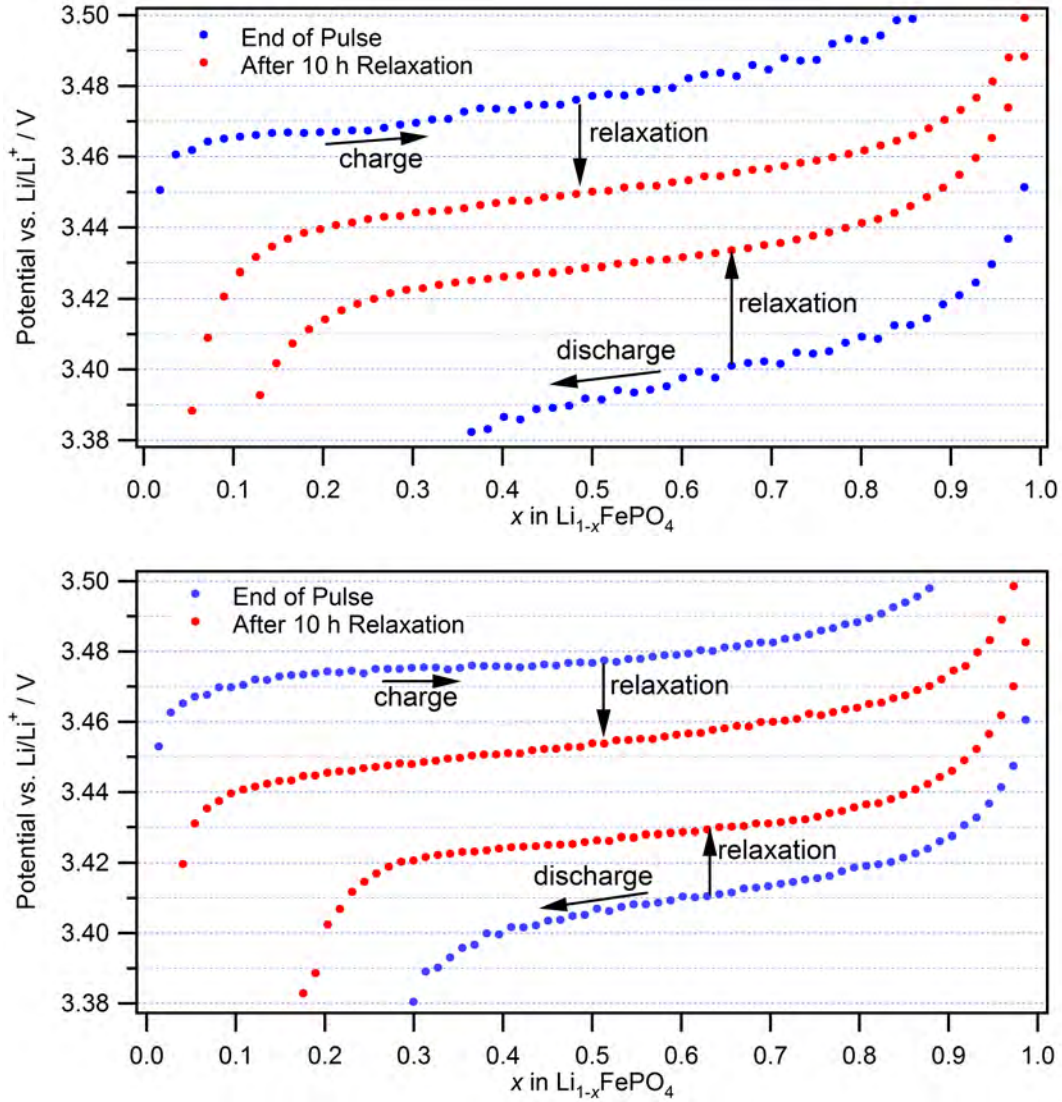


Figure 6.2: The near-equilibrium potentials and the potentials at the end of each charging pulse against the composition. Sample E_LH_111Si113 prepared with 3000 pulses (top) and sample E_LH_111Si75 prepared with 5000 pulses (bottom). The composition was approximated by the total capacity. The top branches of the plots show the potential during charging and the lower branches show the potentials during the discharge cycle.

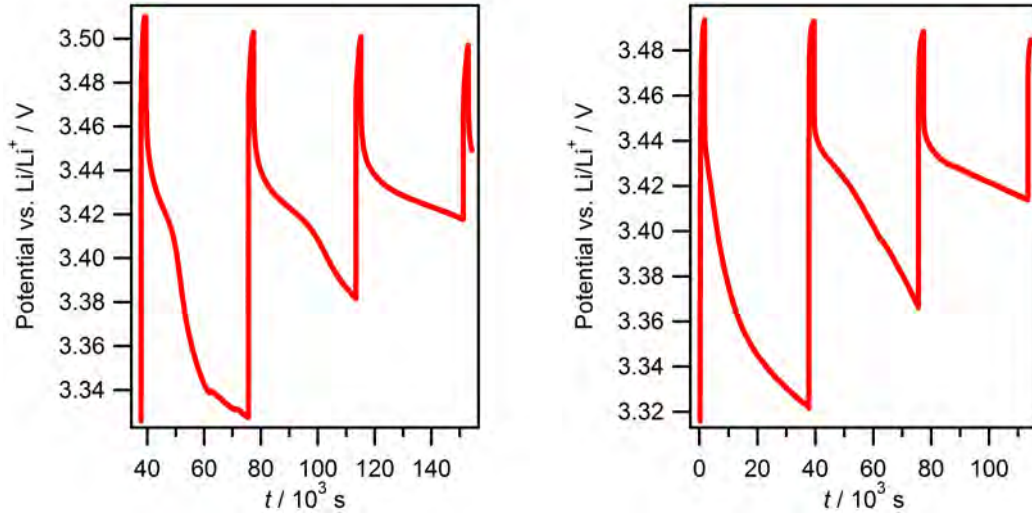


Figure 6.3: Plateau in the relaxation curves after the first few pulses. This feature only appeared in the electrodes deposited at lower temperatures or in relatively thick electrodes. Sample E_LH_111Si47 (left) was deposited at a substrate temperature of 700 °C and with 3000 pulses. Sample E_LH_111Si76 (right) was deposited at a substrate temperature of 800 °C and with 5000 pulses.

The features described above appeared in every measurement, regardless of the electrode thickness. The effect only scaled with the thickness. Another feature occurred only in the thicker electrodes or in electrodes deposited at lower temperatures. During the first steps the potential seems to reach a plateau during relaxation. However, after some time, the potential drops again. This behavior indicates a phase transition. Some of those relaxation curves are shown in figure 6.3.

In order to compare the obtained data with the particle electrodes used in industrial batteries a GITT measurement was conducted on such a sample. The carbon coated LFP-P2 by *Phostech Lithium* was cast onto an aluminum foil with a continuous coating machine by the Institute for Particle Technology at the Technical University Braunschweig. As a binder, PVDF was used and carbon was added for a better electronic conduction. The film thickness was 80 μm . The electrode used in the cell had a diameter of 12 mm. The electrolyte with LiPF_6 in EC/DEC was used for the electrochemical measurement in a three-

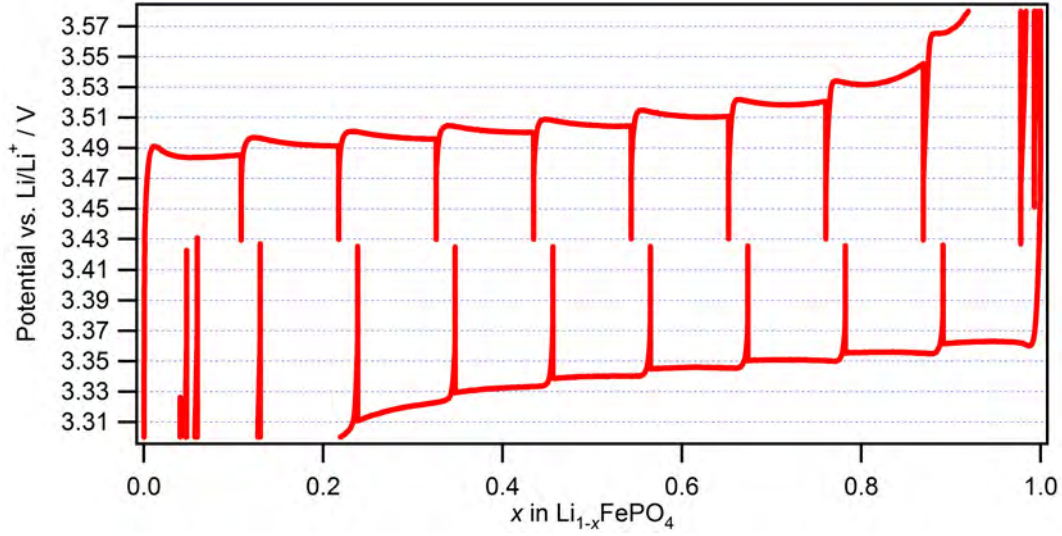


Figure 6.4: GITT measurement of a particle sample. The electrode thickness was 80 μm . The equilibrium potentials exhibit a hysteresis between the charging and the discharging branch of 5 mV. The plateau of the potentials exhibits no slope.

electrode setup. The pulse current was set to 300 μA for a duration of 30 min and a subsequent rest time of 10 h. The plot of the potential versus the composition is shown in figure 6.4. The plateau of the equilibrium voltages exhibits no slope, as predicted by Gibbs' phase rule. The potentials of the charging branch and of the discharging branch exhibit a small hysteresis of about 5 mV, which is probably due to a concentration gradient in the amorphous surface layer of the particles.

6.3 Discussion

A constant voltage plateau would be expected for a two-phase system like LFP. However, this plateau does exhibit a slope for the thin films prepared in this study. As described in section 2.2, it could be shown that the miscibility gap of LFP shrinks with smaller particle size.^[18] An extrapolation of that reduced miscibility gap by Meethong et al. yielded a vanishing gap for a particle size of about 15 nm.^[19] The particle size in the thin films was determined to be

between 10 nm and 20 nm in TEM measurements. This particle size matches the projected size for a vanishing miscibility gap. Thus, the thin film does not show the characteristics of a two-phase systems, but has a lithium miscibility over the entire composition range.

The hysteresis of the near-equilibrium voltage indicates the existence of a concentration gradient inside the electrode. The potential difference between the charging and the discharging cycle is 20 mV to 25 mV. The gradient of the potential at the end of the relaxation step is less than 0.2 mV h^{-1} . Even if one would assume the gradient to stay constant at this low rate, the time to reach the midpoint between both hysteresis over-potentials is more than 50 hours. Reorganization inside of LFP electrodes has been observed before.^[38,39] However, those observations have focused on structural properties, as the studies utilized x-ray diffraction. The present study shows an impact of the structural reorganization onto the electrochemical potential of the electrode. Furthermore, the plateau in the relaxation curve during the first steps indicates a phase transition at that stage. This is particularly noteworthy as, due to the absence of a miscibility gap, a phase transition is not expected. If a phase transition occurs, an intermediate phase must be stable under these conditions with the entire active material transitioning into that structure.

6.4 Explaining the Observed Data

With the application of a current across the system, the delithiation begins in the surface area of the electrode. The lithium ions located deeper inside the electrode must then migrate to the surface. At the end of the current pulse, the surface area will be completely depleted of lithium with a concentration gradient into the material. At a certain position in the electrode, the concentration of the electrode will not have changed during the current pulse. During the subsequent relaxation, the concentration gradient will be reduced in accordance with Fick's laws. The local chemical potential gradient of lithium drives

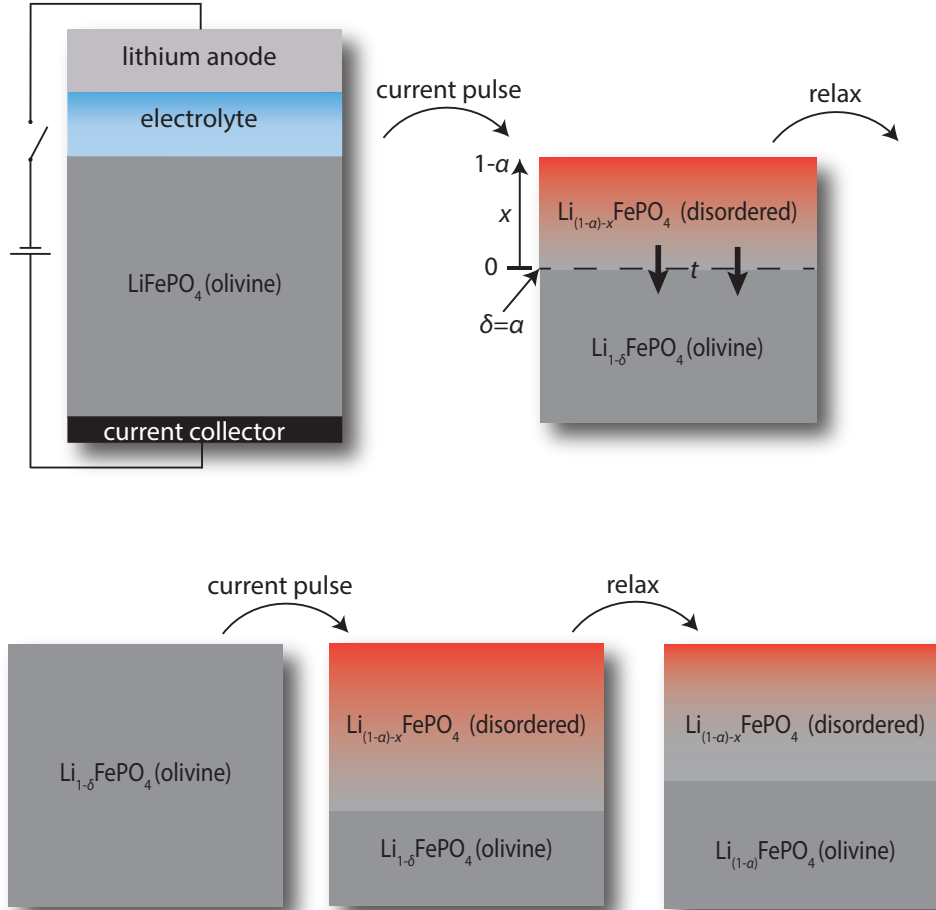


Figure 6.5: Schematic model of the delithiation and the subsequent relaxation process. Initially, the material at the surface is delithiated. The LFP at the surface transitions from the olivine phase to the disordered phase. The concentration gradient is reduced in the subsequent relaxation step. If the lithium content in the remaining olivine material is sufficient, the surface material transitions back from the disordered phase to the olivine phase. After several steps, the overall lithium content is not sufficient to keep the olivine phase stable in the whole electrode and the disordered phase is present at the surface. Even after a long relaxation time, the concentration gradient does not vanish. This is due to the small local potential gradient which is not sufficient to drive the migration toward equilibrium.

this diffusion process. A finite potential gradient will remain even after long relaxation times due to slow diffusion kinetics.

The plateau observed in the first steps only occurred in thick films or in films deposited at lower temperatures. Films with these parameters have an important trait in common. The kinetics are usually slower, either due to the thicker material or due to the larger number of defects. The observed effect may be present in the other electrodes as well, however, can not be observed because of the faster kinetics. The phase transition responsible for this plateau is from a disordered phase with no miscibility gap regarding the lithium content to the ordered olivine phase. After the current pulse led to the phase transition in the surface of the electrode, the concentration gradient is reduced during the relaxation process. During this process, the concentration surpasses the regime in which the disordered phase is stable and the ordered phase forms again in the surface. After some pulses the lithium reservoir is reduced far enough to stay in the concentration regime of the disordered phase. The plateau is not observed in the reverse direction in the discharge cycle, as the reservoir can never be filled completely, because of the permanent concentration gradient after relaxation. Thus, the plateau does also not appear in the second charging cycle.

6.5 Diffusion Coefficient of the Disordered Phase

It has been noted in section 4.4 that the GITT equations are only valid for single-phase systems and are thus not valid for the two-phase lithium iron phosphate. However, the model for the charging and discharging of LFP thin films proposed in the previous section suggests a disordered phase over a large composition range. The disordered phase being a single-phase system allows for an analysis by the GITT method.

Equation 4.16 was used for the analysis. However, the utilized pulse was very long, thus only few pulses showed a linear behavior of the plot of the voltage

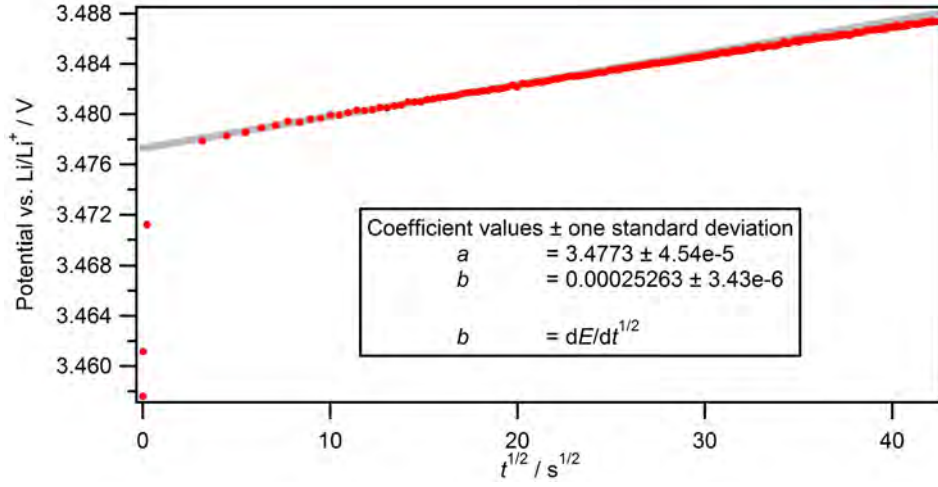


Figure 6.6: Measured potential versus square root of the pulse time. The data were fitted linearly between 20 s and 330 s. The fitted line is shown in gray. The slope of the fitted line gives the value of the term $dE/d\sqrt{t}$ in equation 6.1. The shown pulse is from sample E_LH_111Si113. The composition x in $\text{LiFe}_{1-x}\text{PO}_4$ at the beginning of the pulse was 0.73 during the charging cycle. The polarization of the cell at the beginning of the pulse is about 20 mV.

versus the square root of the time. Accordingly, not the finite quantities of the plot were used for analysis but only the early parts of the pulse. Furthermore, the polarization at the beginning of the pulse had to be eliminated. In order to comply with both conditions a linear fit was applied to the data in the range of 20 s and 330 s. The slope of that fit is the value of the differential term $dE/d\sqrt{t}$. Therefore, equation 6.1 was applied for the data analysis. A plot of the voltage versus the square root of the pulse time is shown in figure 6.6.

$$\tilde{D} = \frac{4}{\pi} \left(\frac{V_M}{S z_i F} \right)^2 \left[I_0 \left(\frac{\Delta E_s}{\Delta \delta} \right) / \frac{dE}{d\sqrt{t}} \right]^2 \quad (6.1)$$

\tilde{D} is the diffusion coefficient, V_M is the molar Volume, S the surface area, z the charge of the mobile species, and F is the Faraday constant. I_0 is the current applied during the pulse, ΔE_s the slope of the near-equilibrium potential, and $\Delta \delta$ is the change of the composition. $dE/d\sqrt{t}$ is the slope of the plot shown in figure 6.6.

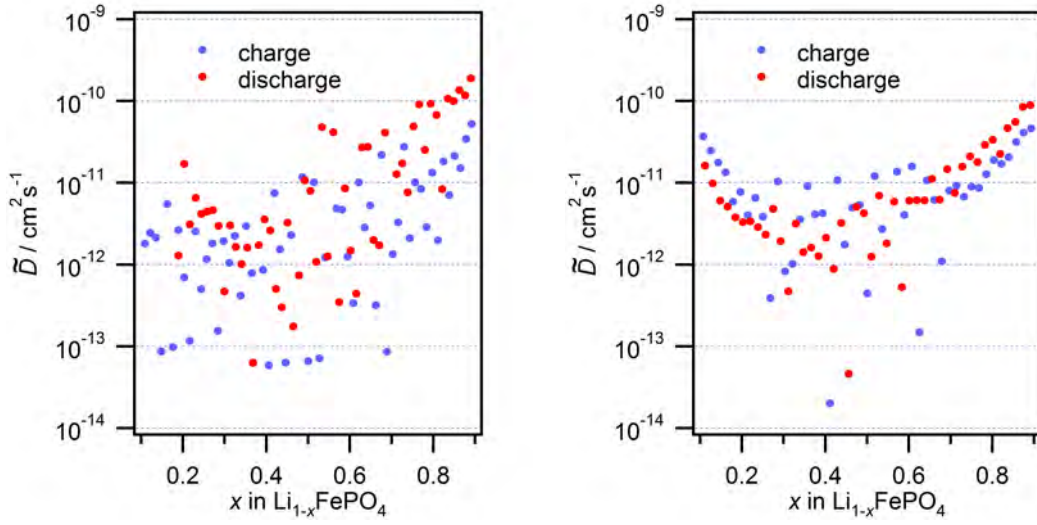


Figure 6.7: Diffusion coefficients of samples E_LH_111Si75 (left) and E_LH_111Si113 (right) calculated by GITT (equation 4.16). The average coefficient for the middle part of the charging branch is $2.8 \times 10^{-12} \text{ cm}^2 \text{ s}^{-1}$ for sample E_LH_111Si75 and $5.3 \times 10^{-12} \text{ cm}^2 \text{ s}^{-1}$ for sample E_LH_111Si113. The mean coefficient of the middle part of the discharging branch is $7.7 \times 10^{-12} \text{ cm}^2 \text{ s}^{-1}$ for sample E_LH_111Si75 and $4.0 \times 10^{-12} \text{ cm}^2 \text{ s}^{-1}$ for sample E_LH_111Si113. The data was averaged for the composition range x from 0.2 to 0.7.

The calculated diffusion coefficients of samples E_LH_111Si75 and E_LH_111Si113 are shown in figure 6.7. The values calculated from the charging branch and the discharging branch of the GITT experiment are both shown in the graphs. At low and high lithium concentrations, a phase transition from the ordered to the disordered phase occurs making that two-phase area not utilizable for GITT. The middle parts of the plots show a constant diffusion coefficient. The data scatters a lot in this part due to the small values of the potential changes. The average diffusion coefficient is between $3 \times 10^{-12} \text{ cm}^2 \text{ s}^{-1}$ and $8 \times 10^{-12} \text{ cm}^2 \text{ s}^{-1}$. The values reported before were between $10^{-15} \text{ cm}^2 \text{ s}^{-1}$ and $10^{-19} \text{ cm}^2 \text{ s}^{-1}$.^[54,68] These very low values were obtained, because the system was still in the two-phase regime. Thus, the term ΔE_s describing the voltage change of the equilibrium potential tends toward zero during the voltage plateau yielding a very low value for the diffusion coefficient.

7 Imaging of the $\text{LiFePO}_4/\text{FePO}_4$ Phase Boundary

The previous chapter focused on the electrochemical properties of LFP thin films. However, a detailed analysis of the mechanisms of lithium insertion and extraction requires imaging techniques for the phase boundaries and concentration gradients. In order to image the phase boundary between lithium iron phosphate and iron phosphate, LFP was deposited onto substrates for x-ray absorption spectroscopy (XAS). A proof-of-principle study has been performed to demonstrate the feasibility of in operando measurements. The beamline specifications are described in section 3.2.

7.1 Deposition of LFP onto X-Ray Transparent Windows

XAS requires an x-ray transparent substrate. Si_3N_4 windows on silicon frames have been obtained from *Silson*. The windows used for the first depositions had a size of 0.5 mm by 0.5 mm and were 200 nm thick. The silicon frames had a size of 5 mm by 5 mm. The films were deposited with a fluence of 3 J cm^{-2} and 1,000 pulses. The substrate temperature was 700 °C.

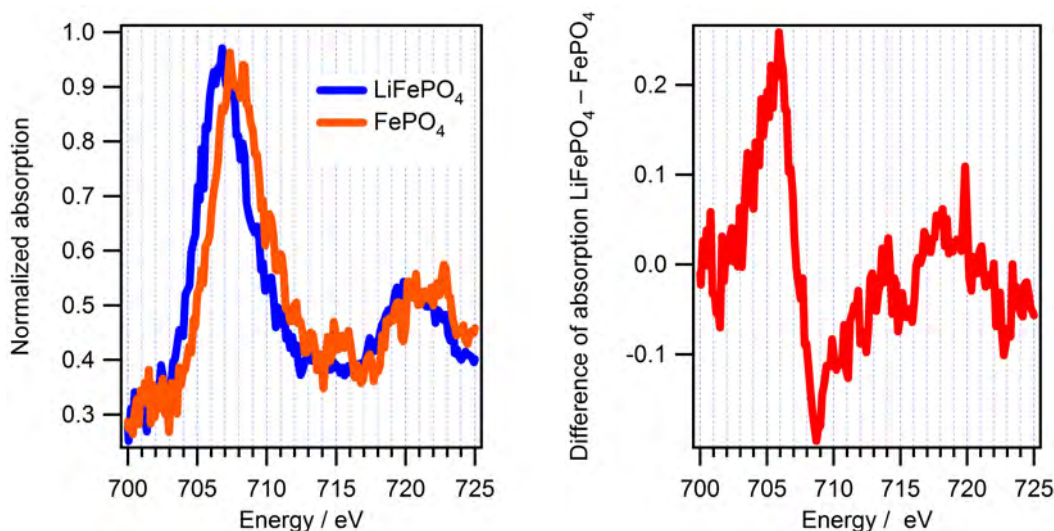


Figure 7.1: Measured XANES spectra of an as-deposited LiFePO_4 sample and a chemically delithiated FePO_4 sample (left). The shift of the Fe-L edge is about 1 eV. Difference of the two spectra (right).

7.2 Image Acquisition

A contrast between the phases is vital in order to image the phase boundary between LiFePO_4 and FePO_4 . Although the results shown in chapter 6 suggest the absence of a phase boundary in thin films, imaging of a concentration gradient may still be possible. Accordingly, lithiated and delithiated samples were prepared. X-ray absorption spectroscopy (XAS) measurements were conducted on these samples at the beamline *TwinMic* at synchrotron *Elettra* in Trieste, Italy. The lithiated samples were as-prepared PLD thin films. Delithiated samples were prepared by chemical delithiation of thin films. The chemical delithiation was achieved by the method described in section 5.2.3. Furthermore, one sample was dipped into the $\text{K}_2\text{S}_2\text{O}_8$ -solution so far as to cover only half the window with the oxidizing solution. The lithium content of the latter sample was imaged using x-ray absorption scanning microscopy.

The delithiated sample had a shift of the Fe-L edge of 1 eV relative to the as-deposited sample. This is just enough to distinguish between the lithiated and the delithiated material. The measured spectra are shown in figure 7.1. The

7 Imaging of the $\text{LiFePO}_4/\text{FePO}_4$ Phase Boundary

peaks of the absorption edges are at about 708 eV and 709 eV. However, the maximum difference between the two spectra is at 706 eV and 709 eV. In order to find the boundary between the lithium rich and the delithiated material, the half delithiated thin film was imaged using the different energies. The images at 706 eV and 709 eV were subtracted from each other in order to maximize the contrast of the image and to reduce morphological effects. Since the field of view was much smaller than the window, several image stacks were recorded over the diagonal along the concentration gradient. The obtained images are shown in figure 7.2. The red parts are FePO_4 and the black parts are LiFePO_4 . The black lines present on the entire image are probably due to structural inhomogeneities in the thin film.

The half delithiated sample exhibits a sufficient contrast between the phase containing lithium and the lithium depleted phase. This contrast can be enhanced by combining the images acquired at two different energies. The resolution of the imaging mode utilized was only 1 μm , hence the coarse grained images. A resolution of 100 nm is possible with another microscope mode of the same beamline. However, this mode has a very small field of view of only 20 μm by 20 μm . Therefore, a cell with similar dimensions has to be structured, in order to confine the process of interest to the area being observed. A concept for such a cell will be presented in the next chapter.

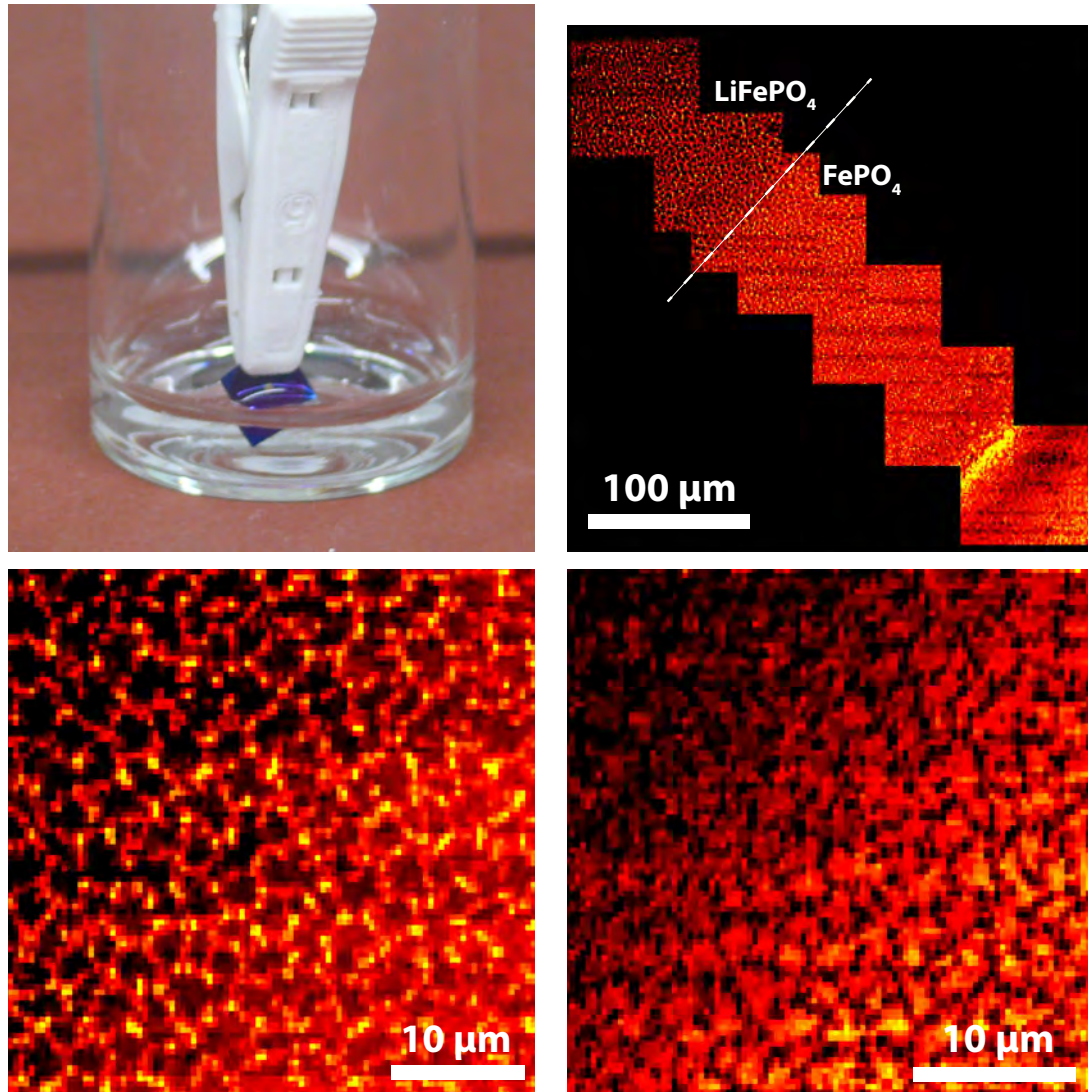


Figure 7.2: Imaging of the phase boundary between FePO_4 and LiFePO_4 . Preparation of the sample with saturated $\text{K}_2\text{S}_2\text{O}_8$ -solution (top left). Images taken at 706 eV along the diagonal crossing the concentration gradient (top right). Image of the concentration gradient at 706 eV (bottom left). Image with optimized contrast by subtracting the image at 709 eV from the image at 706 eV (bottom right). The bottom images are coarse grained due to the low spatial resolution of 1 μm of the acquired data.

8 Outlook - Toward In Operando Microscopy

The results shown in this thesis clearly show that the mechanism of lithiation and delithiation of LFP cannot be revealed by ex situ experiments. Anytime a current is drawn through an electrode, the charging or discharging is followed by a complex and slow relaxation step. Simple electrochemical testing will not suffice to understand those processes. In operando experiments with a good spatial resolution are necessary.

8.1 Requirements for In Operando Studies

In order to conduct in operando studies with a sufficient spatial resolution, some basic requirements have to be met. Firstly, the measurement has to be possible under the working conditions of the cell, e.g. organic electrolytes cannot be used in vacuum chambers. In this example, an ionic liquid or a solid electrolyte has to be used, for a technique requiring vacuum. In some cases cells with special windows can be constructed, making it possible to still use the desired technique. However, this is not possible for any kind of electron spectroscopy as there are no electron transparent windows. Furthermore, the material to be studied has to be stable under the experimental conditions, e.g. the energy input by the laser in Raman spectroscopy can induce a phase transition in LFP.^[61] If care is not taken in this regard, the obtained data may become useless. In addition, the system to be observed must have a sufficient contrast

upon chemical changes being measured. This contrast may be the shift of a peak or an intensity change. Further important requirements are the auxiliary units on the machine being used. If an electrochemical experiment is to be conducted, the machine must have feed throughs for the cables. If the constructed cell is air sensitive, the machine needs to have a transfer mechanism to avoid air contact when introducing the cell.

Since this list is about requirements for in operando studies, an important part is of course the spatial and temporal resolution. The spatial resolution has to be better than the characteristic length of the event being observed. Likewise, the temporal resolution has to be shorter than the time of the process. A big challenge in this regard is that usually neither the size of the spatial domain nor the process time are known.

8.2 In Operando Cells in Literature

Many spectroscopic in operando studies have been conducted on LFP, however, most of those studies did not yield any spatial information. Hard x-ray XAS studies on $\text{Li}_x\text{Fe}_y\text{Mn}_{1-y}\text{PO}_4$ and LFP have been reported by Nedoseykina et al.^[70] and Leriche et al.^[71]. A soft x-ray XAS study has been published by Liu et al.^[72]. Mößbauer and XRD studies were demonstrated by Perea et al.^[73] General cell concepts for IR and Raman spectroscopy have been introduced by Novák et al.^[74]

A spatially resolved in operando study on a pouch cell has been conducted by Siegel et al. utilizing neutron diffraction. However, the spatial resolution was only enough to distinguish between the anode and the cathode and could not be utilized to investigate processes inside the electrodes.^[75] A cell for in operando SEM studies on SnO_2 electrodes was demonstrated by Chen et al. using an ionic liquid as the electrolyte.^[76]

A study on a thin film TiO_2 cathode using AFM was conducted by Zhu et al.^[77]

Photoelectron spectroscopy on a LiCoO_2 thin film cathode was demonstrated by Thißen et al.^[6]

8.3 Lithography for an In Operando Micro Cell

As noted above, in operando microscopy requires a good spatial resolution. However, methods with a good spatial resolution usually only have a small field of view. Thus, it is advantageous if the cell being observed is small itself. This way, the area where the process of interest can take place is reduced. Preparing small structures is possible by means of lithography. Lithographic structuring is possible in two ways. Either the structuring is done by depositing material onto a substrate with a resist that has been previously structured. This step is then followed by a lift-off in the areas with the resist. The other way is to deposit a film onto a substrate and cover the desired structure with a resist. This step is then followed by etching of the non-protected areas. Since the temperatures required for the deposition of LFP are higher than the decomposition temperature of the resists available, only the latter technique can be used for structuring LFP. Another challenge in the construction of in operando cells is the access of active material for the spectroscopic method being used. If the technique uses transmission of electrons or radiation, stacking of the components is not possible. If the technique utilizes reflection or emission from the surface that surface must not be covered by any other material. Nevertheless, all the other components of an electrochemical cell have to be structured into the cell.

First attempts to structure an LFP micro cell onto a Si_3N_4 window were made. LFP was deposited at a substrate temperature of 700°C with a laser fluence of 2 J cm^{-2} and 3,000 pulses. In a clean room $60\text{ }\mu\text{L}$ of Ma-P1215 resist were applied to the substrate and the thickness of the resist was adjusted by spinning at 3,000 rpm for 30 s. This was followed by a soft bake at 100°C for 3 min. The light exposure time for the photoresist was 13 s. The resist was developed for 25 s followed by a hard bake step at 100°C for 45 min. Etching of the LFP thin

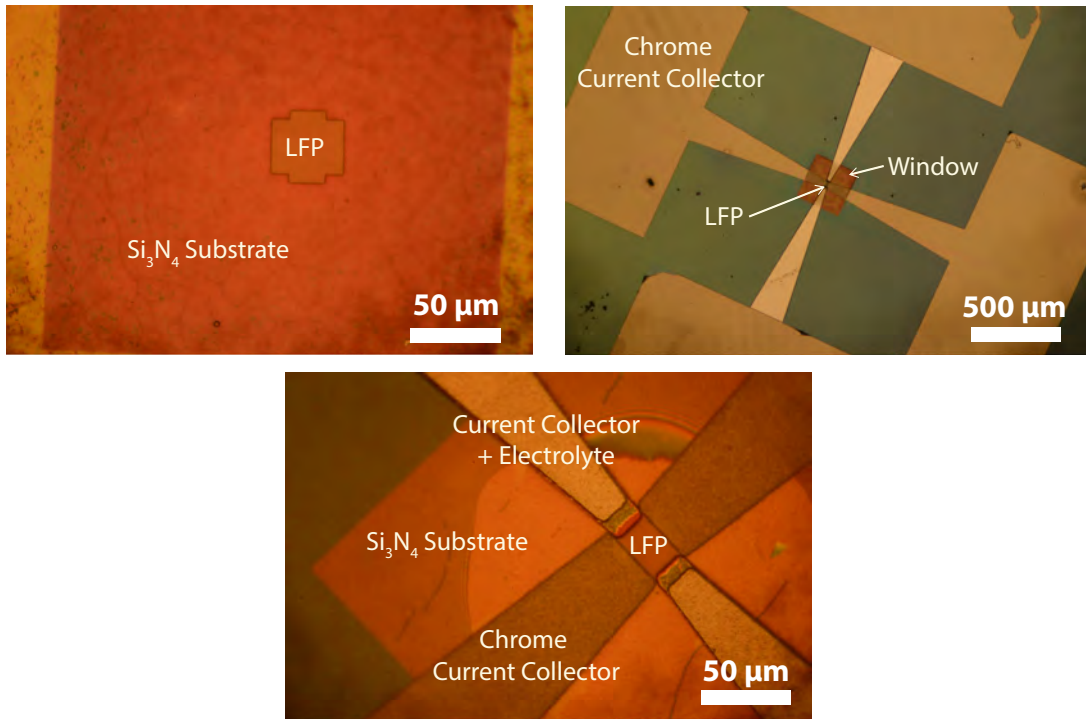


Figure 8.1: Lithographic structuring of an LFP micro cell. Structured LFP thin film (top left). Four current collectors structured toward the LFP with large patches at the edges for contacting (top right). Two of the current collectors are structured onto the LFP and two current collectors leave a gap of about 5 μm which is later filled with solid electrolyte (bottom).

film was done with 10^{-3} M HCl solution in which the substrate was immersed for 3 min. The resulting LFP structure with a size of about $40\text{ }\mu\text{m}$ by $40\text{ }\mu\text{m}$ is shown in figure 8.1.

Structuring of the LFP was followed by structuring of current collectors. Chrome was deposited onto a previously structured photoresist followed by a lift-off step. An electrochemical cell needs two current collectors, one for the anode and one for the cathode. However, four current collectors were structured in order to have a redundant structure in case of a failure. Two of those current collectors were structured onto the edge of the LFP structure. The other two current collectors were structured with a gap of about $5\text{ }\mu\text{m}$ toward the LFP structure. This gap was later filled with a solid electrolyte deposited on top of the current collector closing the gap toward the LFP.

Due to the other materials structured before the deposition of the electrolyte thin film, structuring by etching was not possible. Structuring has thus to be accomplished by lift-off. Accordingly, the solid electrolyte used must be deposited at temperatures below the decomposition temperature of the photoresist. This reduces the available options to amorphous electrolytes deposited at room temperature like LIPON.^[5] After the electrolyte is structured onto the cell, the last missing part is the anode. Lithium metal is not compatible with the resists containing water and the organic developing solutions. Furthermore, the restrictions for the deposition temperature still exist. These conditions do not leave many options. For the first attempts, the anode was omitted completely, as charging of LFP should still be possible with an overpotential for the formation of metallic lithium.

Several micro cells were structured onto Si_3N_4 windows as described above and shown in figure 8.1. Unfortunately, the Si_3N_4 film seems to have cracked during the preparation process. With the current collectors in direct contact with the silicon wafer beneath the Si_3N_4 film, all the cells had a short circuit and could not be charged.

While structuring of a micro cell did not work on a Si_3N_4 window, a more robust substrate may be suitable for this process. While this may exclude many techniques working with transmission through the sample, even XAS measurements are possible on other substrates when using the fluorescence mode.

8.4 Concluding Remarks

The herein presented work shows the vanishing of the miscibility gap in thin films of the two-phase system $\text{FePO}_4/\text{LiFePO}_4$. This effect is expected in particles with a size of less than about 15 nm. TEM images of a thin film showed a particle size of 10 nm to 20 nm which matches the predicted particle size for a vanishing miscibility gap.^[19] Vanishing of the miscibility gap of LFP has

been reported before in particle samples^[78], however, the therein reported potential curves lay well below the equilibrium voltage of LFP. Additionally, only few studies exist reporting the electrochemical relaxation behavior. A report by Meethong et al. showed a significant fraction of the material being present in the disordered phase. However, the particles were still big enough to encounter a partial phase separation.^[37] The data presented here supports the theory of a metastable disordered phase forming as an intermediate phase. If the particle size is small enough, the disordered phase is stable and will not separate into the end-phases. However, in bigger particles there is a miscibility gap and the particles will separate into two phases. The presence of the disordered phase leads to a slope of the potential plateau, as the nano-sized LFP is a single-phase system. The diffusion coefficient of the disordered phase could be determined by GITT measurements to be about $5 \times 10^{-12} \text{ cm}^2 \text{ s}^{-1}$. A hysteresis in the near-equilibrium voltages indicates a stable concentration gradient inside the electrode due to the slow diffusion kinetics.

In addition to the electrochemical experiments, a setup for an in operando micro-cell has been presented. First experiments failed due to cracks in the substrate surface, but further work on this system should lead to a feasible method for spatially resolved in operando spectroscopy on lithium ion batteries.

List of Tables

2.1	Lattice parameters of LiFePO_4 & FePO_4 . Values from Padhi et al. ^[7]	7
2.2	Overview of publications with PLD preparation of LFP thin films.	15
2.3	Stability of conducting salts on various substrates (from Sauvage et al. ^[55]).	16
5.1	Deposition Parameters for thin film preparation on nickel substrates.	36
5.2	Deposition Parameters for thin film preparation on silicon substrates.	38
5.3	Film thicknesses and morphologies of PLD thin films in literature.	50
6.1	Deposition parameters for thin films used for GITT measurements.	52

List of Figures

2.1	Crystal structure of LFP.	7
2.2	Phase diagrams of Li_xFePO_4	9
2.3	Particle structure according to the shrinking-core model.	12
3.1	Schematic setup of a PLD chamber and steps of the ablation process.	18
3.2	Setup of the PLD chamber.	20
3.3	The electrochemical cell used for single crystal substrates.	24
4.1	Illustration of the boundary conditions for the GITT experiment.	29
4.2	The GITT process	31
5.1	XRD patterns and Raman spectra of thin films on nickel substrates.	35
5.2	SEM images of thin films on nickel substrates.	36
5.3	100 galvanostatic cycles of LFP on a nickel substrate.	37
5.4	The difference between electrochemical and chemical delithiation.	39
5.5	XRD patterns of as-deposited and delithiated samples.	41
5.6	Cycling of a chemically delithiated thin film.	42
5.7	SEM images of thin films. Top view and cross section.	43
5.8	Film thickness versus number of pulses used for the deposition and XRDs of films with various thicknesses.	45
5.9	TEM images of sample E_AC_111Si129.	47
5.10	Galvanostatic cycling of thin films on silicon substrates.	48
6.1	Potential versus time of sample E_LH_111Si113 during the GITT experiment.	53

6.2	The near-equilibrium potentials and the potentials at the end of each charging pulse against the composition.	54
6.3	Plateau in the relaxation curves after the first pulses.	55
6.4	GITT measurement of a particle sample.	56
6.5	Schematic model of the delithiation and the subsequent relaxation process.	58
6.6	Potential versus square root of pulse time.	60
6.7	Diffusion coefficients calculated by GITT.	61
7.1	Measured XANES spectra of an as-deposited LiFePO_4 sample and a chemically delithiated FePO_4 sample.	63
7.2	Imaging of the phase boundary between FePO_4 and LiFePO_4 . . .	65
8.1	Lithographic structuring of an LFP micro cell.	69

List of Symbols

δ		stoichiometric coefficient in a phase of the form $A_\delta B$
τ	[s]	pulse duration
\tilde{D}	[m ² /s]	chemical diffusion coefficient
c	[mol/m ³]	concentration
ΔE_t	[V]	voltage difference before and after a pulse
ΔE_s	[V]	difference of the equilibrium voltages between GITT steps
F	[C/mol]	Faraday constant
I	[A]	electrical current
j	[mol/m ² · s]	molar flux through a unit area
L	[m]	electrode thickness
M	[g/mol]	molecular mass or mass of a formular unit
m	[g]	mass
N_A	[1/mol]	Avogadro constant
q	[C]	elementary charge
S	[m ²]	electrode area
t	[s]	time
V_M	[m ³ /mol]	molar volume
x	[m]	position in the film measured from the surface
z		charge number

List of Abbreviations

AFM	atomic force microscopy
CV	cyclic voltammetry
DMC	dimethyl carbonate
DEC	diethyl carbonate
EC	ethylene carbonate
GITT	galvanostatic intermittent titration technique
LiBOB	lithium bis(oxalato)borate
LFP	lithium iron phosphate
PA	post anneal
PLD	pulsed laser deposition
PVDF	polyvinylidene fluoride
RT	room temperature
SEM	scanning electron microscopy
TEM	transmission electron microscopy
XAS	x-ray absorption spectroscopy
XRD	x-ray diffraction

Bibliography

- [1] M. Armand, J.-M. Tarascon, Building better batteries, *Nature* **2008**, 451(7179), 652.
- [2] N. Williard, W. He, C. Hendricks, M. Pecht, Lessons Learned from the 787 Dreamliner Issue on Lithium-Ion Battery Reliability, *Energies* **2013**, 6(9), 4682.
- [3] J. Bates, Fabrication and characterization of amorphous lithium electrolyte thin films and rechargeable thin-film batteries, *Journal of Power Sources* **1993**, 43(1-3), 103.
- [4] J. Bates, G. Gruzalski, N. Dudney, C. Luck, X. Yu, Rechargeable thin-film lithium batteries, *Solid State Ionics* **1994**, 70-71(Part 1), 619.
- [5] J. B. Bates, N. J. Dudney, G. R. Gruzalski, R. A. Zuhr, A. Choudhury, C. F. Luck, J. D. Robertson, Electrical properties of amorphous lithium electrolyte thin films, *Solid State Ionics* **1992**, 53-56(Part 1), 647.
- [6] A. Thißen, D. Ensling, M. Liberatore, Q.-H. Wu, F. J. Fernandez Madrigal, M. S. Bhuvaneswari, R. Hunger, W. Jaegermann, Experimental routes to in situ characterization of the electronic structure and chemical composition of cathode materials for lithium ion batteries during lithium intercalation and deintercalation using photoelectron spectroscopy and related techniques, *Ionics* **2009**, 15(4), 393.
- [7] A. K. Padhi, K. Nanjundaswamy, J. Goodenough, Phospho-olivines as Positive-Electrode Materials for Rechargeable Lithium Batteries, *Journal of The Electrochemical Society* **1997**, 144(4), 1188.

-
- [8] M. S. Islam, D. J. Driscoll, C. A. J. Fisher, P. R. Slater, Atomic-Scale Investigation of Defects, Dopants, and Lithium Transport in the LiFePO_4 Olivine-Type Battery Material, *Chemistry of Materials* **2005**, 17(20), 5085.
- [9] X. Guo, M. Wang, X. Huang, P. Zhao, X. Liu, R. Che, Direct evidence of antisite defects in $\text{LiFe}_{0.5}\text{Mn}_{0.5}\text{PO}_4$ via atomic-level HAADF-EELS, *Journal of Materials Chemistry A* **2013**, 1(31), 8775.
- [10] J. Chen, M. Whittingham, Hydrothermal synthesis of lithium iron phosphate, *Electrochemistry Communications* **2006**, 8(5), 855.
- [11] S. Yang, Y. Song, K. Ngala, P. Y. Zavalij, M. Stanley Whittingham, Performance of LiFePO_4 as lithium battery cathode and comparison with manganese and vanadium oxides, *Journal of Power Sources* **2003**, 119-121, 239.
- [12] S.-Y. Chung, S.-Y. Choi, S. Lee, Y. Ikuhara, Distinct Configurations of Anti-site Defects in Ordered Metal Phosphates: Comparison between LiMnPO_4 and LiFePO_4 , *Physical Review Letters* **2012**, 108(19), 195501.
- [13] J. L. Dodd, R. Yazami, B. Fultz, Phase Diagram of Li_xFePO_4 , *Electrochemical and Solid-State Letters* **2006**, 9(3), A151.
- [14] C. Delacourt, P. Poizot, J.-M. Tarascon, C. Masquelier, The existence of a temperature-driven solid solution in Li_xFePO_4 for $0 \leq x \leq 1$, *Nature Materials* **2005**, 4(3), 254.
- [15] F. Zhou, T. Maxisch, G. Ceder, Configurational Electronic Entropy and the Phase Diagram of Mixed-Valence Oxides: The Case of Li_xFePO_4 , *Physical Review Letters* **2006**, 97(15), 155704.
- [16] M. Gauthier, C. Michot, N. Ravet, M. Duchesneau, J. Dufour, G. Liang, J. Wontcheu, L. Gauthier, D. D. MacNeil, Melt Casting LiFePO_4 , *Journal of The Electrochemical Society* **2010**, 157(4), A453.
- [17] D. Chen, A. Maljuk, C. Lin, Floating zone growth of lithium iron (II) phosphate single crystals, *Journal of Crystal Growth* **2005**, 284(1-2), 86.

- [18] G. Kobayashi, S.-i. Nishimura, M.-S. Park, R. Kanno, M. Yashima, T. Ida, A. Yamada, Isolation of Solid Solution Phases in Size-Controlled Li_xFePO_4 at Room Temperature, *Advanced Functional Materials* **2009**, 19(3), 395.
- [19] N. Meethong, H.-Y. S. Huang, W. C. Carter, Y.-M. Chiang, Size-Dependent Lithium Miscibility Gap in Nanoscale $\text{Li}_{1-x}\text{FePO}_4$, *Electrochemical and Solid-State Letters* **2007**, 10(5), A134.
- [20] C. Delacourt, L. Laffont, R. Bouchet, C. Wurm, J.-B. Leriche, M. Morcrette, J.-M. Tarascon, C. Masquelier, Toward Understanding of Electrical Limitations (Electronic, Ionic) in LiMPO_4 (M = Fe, Mn) Electrode Materials, *Journal of The Electrochemical Society* **2005**, 152(5), A913.
- [21] C. Wang, J. Hong, Ionic/Electronic Conducting Characteristics of LiFePO_4 Cathode Materials, *Electrochemical and Solid-State Letters* **2007**, 10(3), A65.
- [22] N. Ravet, Y. Chouinard, J. Magnan, S. Besner, M. Gauthier, M. Armand, Electroactivity of natural and synthetic triphylite, *Journal of Power Sources* **2001**, 97-98, 503.
- [23] M. S. Whittingham, Lithium Batteries and Cathode Materials, *Chemical Reviews* **2004**, 104(10), 4271.
- [24] W.-J. Zhang, Structure and performance of LiFePO_4 cathode materials: A review, *Journal of Power Sources* **2011**, 196(6), 2962.
- [25] W.-J. Zhang, Comparison of the Rate Capacities of LiFePO_4 Cathode Materials, *Journal of The Electrochemical Society* **2010**, 157(10), A1040.
- [26] A. Andersson, The source of first-cycle capacity loss in LiFePO_4 , *Journal of Power Sources* **2001**, 97-98(1-2), 498.
- [27] V. Srinivasan, J. Newman, Discharge Model for the Lithium Iron-Phosphate Electrode, *Journal of The Electrochemical Society* **2004**, 151(10), A1517.

- [28] V. Srinivasan, J. Newman, Existence of Path-Dependence in the LiFePO_4 Electrode, *Electrochemical and Solid-State Letters* **2006**, 9(3), A110.
- [29] M. A. Roscher, J. Vetter, D. U. Sauer, Characterisation of charge and discharge behaviour of lithium ion batteries with olivine based cathode active material, *Journal of Power Sources* **2009**, 191(2), 582.
- [30] T. Sasaki, Y. Ukyo, P. Novák, Memory effect in a lithium-ion battery, *Nature Materials* **2013**, 12(6), 569.
- [31] G. Chen, X. Song, T. J. Richardson, Electron Microscopy Study of the LiFePO_4 to FePO_4 Phase Transition, *Electrochemical and Solid-State Letters* **2006**, 9(6), A295.
- [32] L. Laffont, C. Delacourt, P. Gibot, M. Y. Wu, P. Kooyman, C. Masquelier, J. M. Tarascon, Study of the $\text{LiFePO}_4/\text{FePO}_4$ Two-Phase System by High-Resolution Electron Energy Loss Spectroscopy, *Chemistry of Materials* **2006**, 18(23), 5520.
- [33] C. Delmas, M. Maccario, L. Croguennec, F. Le Cras, F. Weill, Lithium deintercalation in LiFePO_4 nanoparticles via a domino-cascade model, *Nat Mater* **2008**, 7(8), 665.
- [34] G. Brunetti, D. Robert, P. Bayle-Guillemaud, J. L. Rouvière, E. F. Rauch, J. F. Martin, J. F. Colin, F. Bertin, C. Cayron, Confirmation of the Domino-Cascade Model by $\text{LiFePO}_4/\text{FePO}_4$ Precession Electron Diffraction, *Chem. Mater.* **2011**, 23(20), 4515.
- [35] C. Ramana, A. Mauger, F. Gendron, C. Julien, K. Zaghib, Study of the Li-insertion/extraction process in $\text{LiFePO}_4/\text{FePO}_4$, *Journal of Power Sources* **2009**, 187(2), 555.
- [36] R. Malik, F. Zhou, G. Ceder, Kinetics of non-equilibrium lithium incorporation in LiFePO_4 , *Nat Mater* **2011**, 10(8), 587.

- [37] N. Meethong, Y.-H. Kao, M. Tang, H.-Y. Huang, W. C. Carter, Y.-M. Chiang, Electrochemically Induced Phase Transformation in Nanoscale Olivines $\text{Li}_{1-x}\text{MPO}_4$ ($\text{M} = \text{Fe}, \text{Mn}$), *Chemistry of Materials* **2008**, 20(19), 6189.
- [38] S. Park, K. Kameyama, T. Yao, Relaxation Crystal Analysis of LiFePO_4 Cathode for Li-Ion Secondary Battery, *Electrochemical and Solid-State Letters* **2012**, 15(4), A49.
- [39] K. T. Lee, W. H. Kan, L. F. Nazar, Proof of Intercrystallite Ionic Transport in LiMPO_4 Electrodes ($\text{M} = \text{Fe}, \text{Mn}$), *Journal of the American Chemical Society* **2009**, 131(17), 6044.
- [40] Y. Iriyama, M. Yokoyama, C. Yada, S.-K. Jeong, I. Yamada, T. Abe, M. Inaba, Z. Ogumi, Preparation of LiFePO_4 Thin Films by Pulsed Laser Deposition and Their Electrochemical Properties, *Electrochemical and Solid-State Letters* **2004**, 7(10), A340.
- [41] F. Sauvage, E. Baudrin, M. Morcrette, J.-M. Tarascon, Pulsed Laser Deposition and Electrochemical Properties of LiFePO_4 Thin Films, *Electrochemical and Solid-State Letters* **2004**, 7(1), A15.
- [42] F. Sauvage, E. Baudrin, L. Gengembre, J.-M. Tarascon, Effect of texture on the electrochemical properties of LiFePO_4 thin films, *Solid State Ionics* **2005**, 176(23-24), 1869.
- [43] C. Yada, Y. Iriyama, S.-K. Jeong, T. Abe, M. Inaba, Z. Ogumi, Electrochemical properties of LiFePO_4 thin films prepared by pulsed laser deposition, *Journal of Power Sources* **2005**, 146(1-2), 559.
- [44] S.-W. Song, R. P. Reade, R. Kostecki, K. A. Striebel, Electrochemical Studies of the LiFePO_4 Thin Films Prepared with Pulsed Laser Deposition, *Journal of The Electrochemical Society* **2006**, 153(1), A12.
- [45] F. Sauvage, E. Baudrin, L. Laffont, J.-M. Tarascon, Origin of electrochemical reactivity enhancement of post-annealed LiFePO_4 thin films: Preparation of heterosite-type FePO_4 , *Solid State Ionics* **2007**, 178(1-2), 145.

-
- [46] Z. G. Lu, M. F. Lo, C. Y. Chung, Pulse Laser Deposition and Electrochemical Characterization of LiFePO_4 -C Composite Thin Films, *The Journal of Physical Chemistry C* **2008**, 112(17), 7069.
- [47] T. Matsumura, N. Imanishi, A. Hirano, N. Sonoyama, Y. Takeda, Electrochemical performances for preferred oriented PLD thin-film electrodes of $\text{LiNi}_{0.8}\text{Co}_{0.2}\text{O}_2$, LiFePO_4 and LiMn_2O_4 , *Solid State Ionics* **2008**, 179(35-36), 2011.
- [48] F. Sauvage, J. Tarascon, E. Baudrin, Insights into the potentiometric response behaviour vs. Li^+ of LiFePO_4 thin films in aqueous medium, *Analytica Chimica Acta* **2008**, 622(1-2), 163.
- [49] J. Sun, K. Tang, X. Yu, H. Li, X. Huang, Needle-like LiFePO_4 thin films prepared by an off-axis pulsed laser deposition technique, *Thin Solid Films* **2009**, 517(8), 2618.
- [50] K. Tang, J. Sun, X. Yu, H. Li, X. Huang, Electrochemical performance of LiFePO_4 thin films with different morphology and crystallinity, *Electrochimica Acta* **2009**, 54(26), 6565.
- [51] C. Legrand, L. Dupont, K. Tang, H. Li, X. Huang, E. Baudrin, Structural and textural characterization of LiFePO_4 thin films prepared by pulsed laser deposition on Si substrates, *Thin Solid Films* **2010**, 518(19), 5447.
- [52] V. Palomares, I. Ruiz de Larramendi, J. Alonso, M. Bengoechea, A. Goñi, O. Miguel, T. Rojo, LiFePO_4 thin films grown by pulsed laser deposition: Effect of the substrate on the film structure and morphology, *Applied Surface Science* **2010**, 256(8), 2563.
- [53] C. Legrand, L. Dupont, C. Davoisne, F. Le Marrec, J. Perrière, E. Baudrin, Unexpected formation by pulsed laser deposition of nanostructured Fe/olivine thin films on MgO substrates, *Journal of Solid State Chemistry* **2011**, 184(2), 351.
- [54] K. Tang, X. Yu, J. Sun, H. Li, X. Huang, Kinetic analysis on LiFePO_4 thin films by CV, GITT, and EIS, *Electrochimica Acta* **2011**, 56(13), 4869.

- [55] F. Sauvage, L. Laffont, J.-M. Tarascon, E. Baudrin, Factors affecting the electrochemical reactivity vs. lithium of carbon-free LiFePO_4 thin films, *Journal of Power Sources* **2008**, 175(1), 495.
- [56] A. Inam, M. S. Hegde, X. D. Wu, T. Venkatesan, P. England, P. F. Miceli, E. W. Chase, C. C. Chang, J. M. Tarascon, J. B. Wachtman, As-deposited high T_c and J_c superconducting thin films made at low temperatures, *Applied Physics Letters* **1988**, 53(10), 908.
- [57] R. Eason, *Pulsed laser deposition of thin films: applications-led growth of functional materials*, Wiley-Interscience, Hoboken, N.J., **2007**.
- [58] M. Stafe, A. Marcu, N. Puscas, B. Benjamin, *Pulsed Laser Ablation of Solids: Basics, Theory and Applications*, Springer, **2013**.
- [59] C. Korte, Habilitation Thesis, JLU Gießen, Gießen, **2008**.
- [60] P. Schichtel, Präparation von LiFePO_4 basierten Dünnschichten und deren strukturelle und elektrochemische Charakterisierung, *Bachelor Thesis*, JLU Gießen, Gießen, **2011**.
- [61] C. M. Burba, J. M. Palmer, B. S. Holinsworth, Laser-induced phase changes in olivine FePO_4 : a warning on characterizing LiFePO_4 -based cathodes with Raman spectroscopy, *Journal of Raman Spectroscopy* **2009**, 40(2), 225.
- [62] B. Kaulich, P. Thibault, A. Gianoncelli, M. Kiskinova, Transmission and emission x-ray microscopy: operation modes, contrast mechanisms and applications, *Journal of Physics: Condensed Matter* **2011**, 23(8), 083002.
- [63] R. S. Nicholson, I. Shain, Theory of stationary electrode polarography. Single scan and cyclic methods applied to reversible, irreversible, and kinetic systems., *Analytical Chemistry* **1964**, 36(4), 706.
- [64] C. Ho, I. D. Raistrick, R. A. Huggins, Application of A-C Techniques to the Study of Lithium Diffusion in Tungsten Trioxide Thin Films, *Journal of The Electrochemical Society* **1980**, 127(2), 343.

- [65] W. Weppner, R. A. Huggins, Determination of the Kinetic Parameters of Mixed-Conducting Electrodes and Application to the System Li_3Sb , *Journal of the Electrochemical Society* **1977**, 124(10), 1569.
- [66] G. Beck, J. Janek, Coulometric titration at low temperatures-nonstoichiometric silver selenide, *Solid State Ionics* **2004**, 170(1-2), 129.
- [67] J. Crank, *The mathematics of diffusion*, Clarendon Press, Oxford, [Eng], **1975**.
- [68] P. Prosini, Determination of the chemical diffusion coefficient of lithium in LiFePO_4 , *Solid State Ionics* **2002**, 148(1-2), 45.
- [69] A. Mauger, C. Julien, Surface modifications of electrode materials for lithium-ion batteries: status and trends, *Ionics* **2014**, 20(6), 751.
- [70] T. Nedoseykina, M. G. Kim, S.-A. Park, H.-S. Kim, S.-B. Kim, J. Cho, Y. Lee, In situ X-ray absorption spectroscopic study for the electrochemical delithiation of a cathode $\text{LiFe}_{0.4}\text{Mn}_{0.6}\text{PO}_4$ material, *Electrochimica Acta* **2010**, 55(28), 8876.
- [71] J. B. Leriche, S. Hamelet, J. Shu, M. Morcrette, C. Masquelier, G. Ouvrard, M. Zerrouki, P. Soudan, S. Belin, E. Elkaïm, F. Baudalet, An Electrochemical Cell for Operando Study of Lithium Batteries Using Synchrotron Radiation, *Journal of The Electrochemical Society* **2010**, 157(5), A606.
- [72] X. Liu, D. Wang, G. Liu, V. Srinivasan, Z. Liu, Z. Hussain, W. Yang, Distinct charge dynamics in battery electrodes revealed by in situ and operando soft X-ray spectroscopy, *Nature Communications* **2013**, 4.
- [73] A. Perea, M. T. Sougrati, C. M. Ionica-Bousquet, B. Fraisse, C. Tessier, L. Aldon, J.-C. Jumas, Operando ^{57}Fe Mössbauer and XRD investigation of $\text{Li}_x\text{Mn}_y\text{Fe}_{1-y}\text{PO}_4/\text{C}$ composites ($y = 0; 0.25$), *RSC Adv.* **2012**, 2(5), 2080.
- [74] P. Novák, J. C. Panitz, F. Joho, M. Lanz, R. Imhof, M. Coluccia, Advanced in situ methods for the characterization of practical electrodes in lithium-ion batteries, *Journal of Power Sources* **2000**, 90(1), 52.

- [75] J. B. Siegel, X. Lin, A. G. Stefanopoulou, D. S. Hussey, D. L. Jacobson, D. Gorsich, Neutron Imaging of Lithium Concentration in LFP Pouch Cell Battery, *Journal of The Electrochemical Society* **2011**, 158(5), A523.
- [76] D. Chen, S. Indris, M. Schulz, B. Gamer, R. Mönig, In situ scanning electron microscopy on lithium-ion battery electrodes using an ionic liquid, *Journal of Power Sources* **2011**, 196(15), 6382.
- [77] J. Zhu, J. Feng, L. Lu, K. Zeng, In situ study of topography, phase and volume changes of titanium dioxide anode in all-solid-state thin film lithium-ion battery by biased scanning probe microscopy, *Journal of Power Sources* **2012**, 197(0), 224.
- [78] T. Ichitsubo, T. Doi, K. Tokuda, E. Matsubara, T. Kida, T. Kawaguchi, S. Yagi, S. Okada, J.-i. Yamaki, What determines the critical size for phase separation in LiFePO_4 in lithium ion batteries?, *Journal of Materials Chemistry A* **2013**, 1(46), 14532.